



Characteristic parameterizations of surfaces with a constant ratio of principal curvatures[☆]

Hui Wang, Helmut Pottmann*

Visual Computing Center, KAUST, Thuwal 23955-6900, Saudi Arabia



ARTICLE INFO

Article history:

Received 6 October 2021

Received in revised form 12 March 2022

Accepted 13 March 2022

Available online 18 March 2022

Keywords:

Discrete differential geometry

Architectural geometry

Weingarten surface

Characteristic parameterization

Constant ratio of principal curvatures

Principal symmetric net

ABSTRACT

Motivated by applications in architectural geometry, we study and compute surfaces with a constant ratio of principal curvatures (CRPC surfaces) based on their characteristic parameterizations. For negative Gaussian curvature K , these parameterizations are asymptotic. For positive K they are conjugate and symmetric with respect to the principal curvature directions. CRPC surfaces are described by characteristic parameterizations whose parameter lines form a constant angle. We use them to derive characteristic parameterizations of rotational CRPC surfaces in a simple geometric way. Pairs of such surfaces with principal curvature ratio $\kappa_1/\kappa_2 = \pm a$ can be seen as equilibrium shapes and reciprocal force diagrams of each other. We then introduce discrete CRPC surfaces, expressed via discrete isogonal characteristic nets, and show how to efficiently compute them through numerical optimization. In particular, we derive discrete helical and spiral CRPC surfaces. We provide various ways how these and other special types of CRPC surfaces can serve as a basis for computational design of more general CRPC surfaces. Our computational tools may also serve as an experimental basis for mathematical studies of the largely unexplored class of CRPC surfaces.

© 2022 Elsevier B.V. All rights reserved.

1. Introduction

The present paper has been motivated by applications in Architectural Geometry. There, one goal is the design of surfaces that have an appearance of freeform shapes, but possess properties which facilitate their construction. An important part of fabrication concerns the cladding with panels. If those are doubly curved and their fabrication therefore requires the use of a mold, it is an advantage to have a small number of molds. One way to achieve this is by a reduced number of curvature elements. This happens if the surface possesses a relation between its principal curvatures κ_1, κ_2 . These surfaces are called *Weingarten surfaces*, studied first by Weingarten (1861) in the same paper in which he introduced the shape operator. The advantage of Weingarten surfaces for paneling architectural freeform surfaces has recently been confirmed in several contributions (Pellis et al., 2020, 2021a,b). There are also arguments for structural advantages of certain types of Weingarten surfaces (Tellié, 2020).

The surfaces studied in the present paper also emerged through special architectural structures, called *asymptotic grid-shells* (Jiang et al., 2020; Schling et al., 2018; Schling, 2018). They are fabricated by bending flat straight lamellas, which in their final position are orthogonal to an underlying smooth surface on which they follow asymptotic curves (Fig. 22).

[☆] Editor: Konrad Polthier.

* Corresponding author.

E-mail addresses: hui.wang.1@kaust.edu.sa (H. Wang), helmut.pottmann@kaust.edu.sa (H. Pottmann).

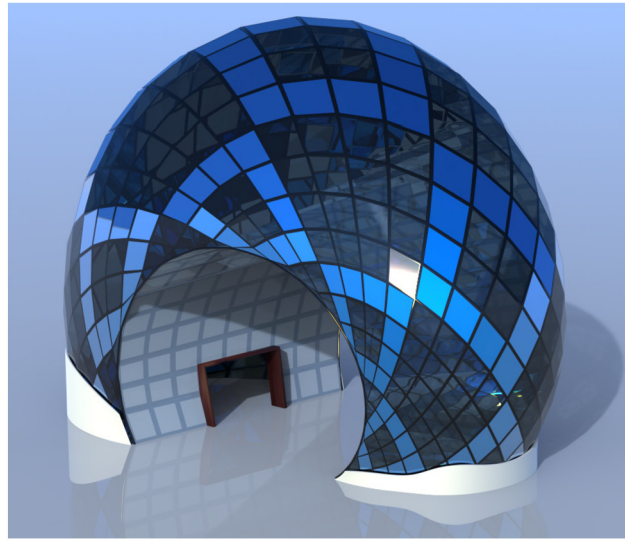


Fig. 1. Architectural design study exhibiting a structure from planar panels based on a discrete CRPC surface with $a = 0.45$. The constant node angle ($\neq \pi/2$) and the principal symmetric arrangement lead to a more interesting visual appearance than a mesh aligned with principal curvature directions would have.

If one requires in addition a constant angle at nodes, these structures realize surfaces whose asymptotic directions form a constant angle, i.e. $\kappa_1/\kappa_2 = a = \text{const.} < 0$. Hence, they are special Weingarten surfaces, namely *surfaces with a constant ratio of principal curvatures (CRPC surfaces)*. Also the positively curved CRPC surfaces are of interest in architecture. This is not only true because of cost effective paneling with double curved panels. Our discrete versions of them provide visually attractive meshes with planar faces, suitable for realization as steel glass structures (Fig. 1).

Interestingly, CRPC surfaces are related to yet another topic in architectural geometry, namely the so-called Caravel meshes of Tellier et al. (2020). In an asymptotic analysis of Caravel quad meshes and Caravel hexagonal meshes with edge offsets, the principal curvature ratio appears in the aspect ratio of faces, so that CRPC surfaces give rise to particularly well balanced Caravel meshes.

Applications mainly benefit from effective computational models, often based on discrete differential geometry (Bobenko and Suris, 2008). From this perspective, Jimenez et al. (2020) studied discrete CRPC surfaces, obtaining discrete principal parameterizations through a novel Christoffel-type transformation of certain spherical nets. They also addressed the case of discrete asymptotic parameterizations (A-nets), but based it on a discrete angle condition which is less effective than the ones used in our work.

CRPC surfaces are a natural generalization of minimal surfaces and thus deserve interest from a purely geometric perspective. While there is a huge body of knowledge on minimal surfaces, very little is known about CRPC surfaces. Explicit parameterizations are only available for rotational CRPC surfaces (Hopf, 1951; Kühnel, 2013; Mladenov and Oprea, 2003, 2007; Lopez and Pampano, 2020). We especially point to a recent paper by Lopez and Pampano (2020) which contains a classification of all surfaces with a linear relation $\kappa_1 = a\kappa_2 + b$ between principal curvatures, including a study of the special case $b = 0$ of rotational CRPC surfaces. The authors also provide a variational characterization of the profiles of these surfaces. Rotational CRPC surfaces with $K < 0$ have also been characterized via isogonal asymptotic parameterizations $f(u, v)$ where $\|f_u\| = \|f_v\|$ (Riveros and Corro, 2012, 2013; Stäckel, 1896). For Weingarten surfaces to a linear relation of the form $a\kappa_1 + b\kappa_2 + c = 0$, it has been shown that they are rotational if they are foliated by a family of circles (López, 2008).

1.1. Contributions and overview

We study CRPC surfaces with help of their characteristic parameterizations, called C-nets henceforth, both in the smooth and in the discrete setting. For Gaussian curvature $K < 0$, C-nets are asymptotic nets (A-nets). For $K > 0$, they are those conjugate parameterizations which are symmetric with respect to the principal directions. Since the curves in a C-net form the angle $\gamma = \arctan \sqrt{|\kappa_1/\kappa_2|}$ with the first principal direction, the CRPC property is simply expressed by a constant angle between the curves in a C-net. Thus, we look for *isogonal C-nets*.

In Section 2, we derive rotational CRPC surfaces in a new way, namely with help of their characteristic curves. This is done via their spherical tangent images and leads to an explicit parameterization with an elementary polar coordinate representation of the axis-parallel projections of the characteristic curves. We also study pairs of rotational CRPC surfaces to $\kappa_1/\kappa_2 = \pm a$ and show that their C-nets are reciprocal force diagrams of each other, implying that the surfaces are membranes in equilibrium and pairs of relative minimal surfaces. We illustrate our results by interesting algebraic rotational CRPC surfaces. One may obtain the characteristic parameterizations also by solving their differential equation based on the known parameterization of rotational CRPC surfaces found first by Hopf (1951) that uses the profiles in planes through

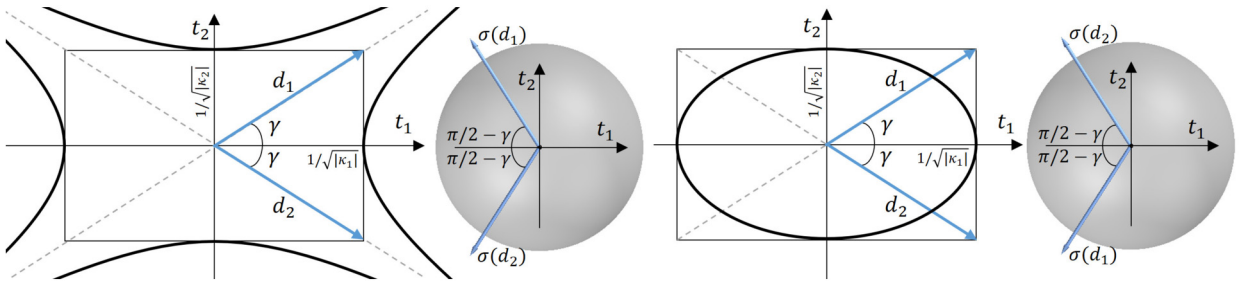


Fig. 2. Characteristic directions visualized via Dupin indicatrix and shape operator for $K < 0$ (left) and $K > 0$ (right).

the rotational axis. However, we believe it is more natural in the present context to derive them directly, since we obtain interesting and simple geometric insights that have not been noted so far in the literature. Moreover, we use the characteristic parameterization later to initialize optimization algorithms for computing more general CRPC surfaces and for quality assessment of our discretization.

Section 3 is devoted to *discrete CRPC surfaces* based on discrete isogonal C-nets. From a computational perspective, these are special constrained quad meshes which can be computed effectively with a numerical optimization algorithm. In particular, we show how to compute discrete CRPC surfaces which are invariant under uniform motions in the group Euclidean similarities. This extends the previously discussed rotational CRPC surfaces towards helical and spiral CRPC surfaces. The main method for their generation relies on the availability of natural discrete surface normals and the use of line geometry or line element geometry on the set of surface normals to express invariance under uniform motions in the group of similarities.

In Section 4 we provide a variety of examples which demonstrate the quality of the obtained surfaces and the effectiveness of numerical optimization. We present ways how the provided algorithms can be used as a design tool for CRPC surfaces and demonstrate this at hand of some examples that are targeted towards architectural applications.

Finally, we address directions for future research. Those need not only be in an applied setting. The presented computational tools could also serve as a basis for getting conjectures and hopefully also theoretical results on CRPC surfaces. We address some directions into which one might go.

2. The characteristic curves of rotational CRPC surfaces

2.1. Characteristic parameterizations

We first consider general CRPC surfaces via their characteristic parameterizations (C-nets).

Let (κ_i, \mathbf{t}_i) , $i = 1, 2$, be the pairs of principal curvatures and associated curvature directions at a surface point p . Then, the directions which form the angles $\pm\gamma$,

$$\tan \gamma = \sqrt{|\kappa_1/\kappa_2|},$$

with \mathbf{t}_1 are called *characteristic directions* henceforth. In case of negative Gaussian curvature K , the characteristic directions are the *asymptotic directions*. For $K > 0$, these are exactly those directions which are conjugate to each other and symmetric with respect to the principal curvature directions.

For visualization, we may use the Dupin indicatrix i_p , whose equation in the principal frame is given by $\kappa_1 x_1^2 + \kappa_2 x_2^2 = \pm 1$ (Fig. 2). Then, for $K < 0$ the characteristic tangents are the asymptotes of the two hyperbolas which form i_p , while for $K > 0$ they are the diagonals in the axis rectangle of the ellipse i_p .

The characteristic directions form the angle $2\gamma = 2 \arctan \sqrt{|\kappa_1/\kappa_2|}$, which may be called *characteristic angle*. This angle characterizes the shape of the curvature element (osculating paraboloid) up to similarities.

Let us take an arbitrary regular point p of a surface. The shape operator σ maps the principal directions \mathbf{t}_i , $\|\mathbf{t}_i\| = 1$, to $\sigma(\mathbf{t}_i) = -\kappa_i \mathbf{t}_i$. Hence, the characteristic directions \mathbf{d}_j , which form the angle γ with \mathbf{t}_1 , are mapped as follows (Fig. 2):

$$\mathbf{d}_j = \frac{1}{\sqrt{|\kappa_1|}} \mathbf{t}_1 \pm \frac{1}{\sqrt{|\kappa_2|}} \mathbf{t}_2 \mapsto \sigma(\mathbf{d}_j) = -\text{sgn}(\kappa_1) \sqrt{|\kappa_1|} \mathbf{t}_1 \mp \text{sgn}(\kappa_2) \sqrt{|\kappa_2|} \mathbf{t}_2.$$

Hence, the two vectors $\sigma(\mathbf{d}_j)$ form the angle γ with the other principal direction \mathbf{t}_2 . For $K < 0$, $\sigma(\mathbf{d}_j)$ is orthogonal to \mathbf{d}_j . For $K > 0$, $\sigma(\mathbf{d}_1)$ ($\sigma(\mathbf{d}_2)$) is orthogonal to \mathbf{d}_2 (\mathbf{d}_1 , resp.). This is just another way to express that the directions $\mathbf{d}_1, \mathbf{d}_2$ are self-conjugate for $K < 0$ and conjugate to each other for $K > 0$.

Through integration of the characteristic directions we get the network of *characteristic curves*. They are the isoparameter curves of *characteristic parameterizations* or *C-nets*.

By their definition, *CRPC surfaces* are those with a constant characteristic angle, or in other words, are characterized through isogonal C-nets. Clearly, their curvature elements (osculating paraboloids and Dupin indicatrices), are similar to each other.

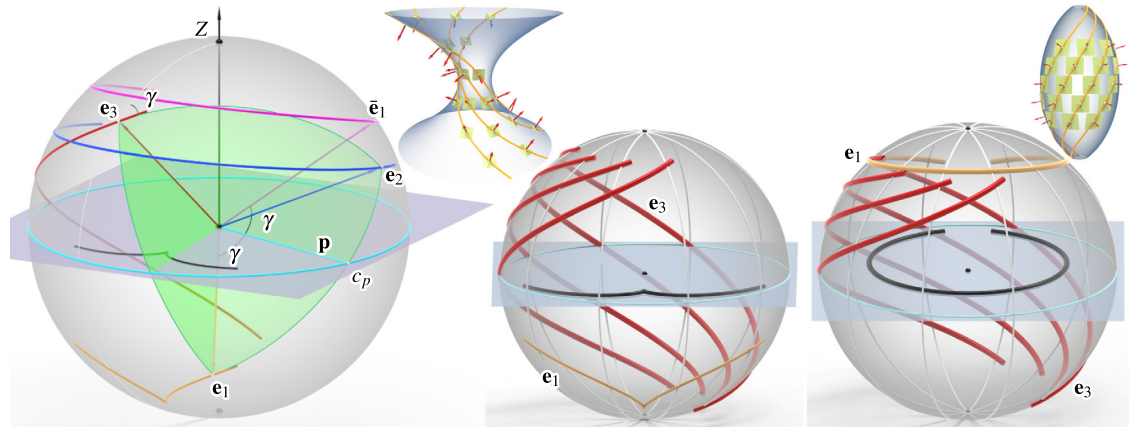


Fig. 3. Spherical tangent and binormal images of characteristic curves on rotational CRPC surfaces. Left: Spherical motion of the Frenet frame $\mathbf{e}_1, \mathbf{e}_2, \mathbf{e}_3$ of an asymptotic curve of a rotational CRPC surface (here $a = -2$): The tangent vector \mathbf{e}_1 generates a spherical tractrix (pull distance γ) of a great circle c_p in a plane orthogonal to the rotation axis of the surface. The binormals \mathbf{e}_3 run on a spherical loxodrome which intersects the great circles through the rotation axis under the angle γ . Center and right: Spherical loxodromes (red) as binormal images and Gaussian images of selected characteristic curves, and a tangent image \mathbf{e}_1 (plus projection into the horizontal plane) in case of negative curvature (middle, $a = -2$) and positive curvature (right, $a = 3$). (For interpretation of the colors in the figure(s), the reader is referred to the web version of this article.)

Characteristic directions are not well defined at umbilics, including flat points. Hence, the *combinatorial singularities of C-nets* appear at these points, which are of course also the singularities of principal parameterizations. A flat point $\kappa_1 = \kappa_2 = 0$ does not pose a restriction for a CRPC surface due to the indeterminate ratio $\kappa_1/\kappa_2 = 0/0$, which can assume the correct value a when approaching such a point. Since negatively curved surfaces have their singularities of the principal nets at flat points, CRPC surfaces with $a < 0$ appear to be easier to design than those with $a > 0$. Also note that the rich family of minimal surfaces ($a = -1$) is part of this class of surfaces. However, we do not know of a similarly rich class of CRPC surfaces with positive curvature. The case $a = 1$ leads just to the sphere. A CRPC surface with $a > 0$ cannot have an umbilic ($a = 1$) unless it is a sphere. This poses a rather strong shape restriction on CRPC surfaces for $a > 0$. They may, however, possess flat points or singular umbilics ($\kappa_1 = \kappa_2 = \infty$). These points appear on the rotational axis of positively curved CRPC surfaces of revolution (see Fig. 5).

2.2. Gaussian image of the C-nets of rotational CRPC surfaces

For an arbitrary CRPC surface \mathbf{s} , the characteristic curves intersect the principal curvature lines under the constant angle $\pm\gamma$. Hence, their Gaussian images intersect the Gaussian images of the principal curvature lines under the constant angle $\pi/2 - \gamma$ (if angles are measured against the same principal direction).

This simple observation turns out to be very useful to directly determine the characteristic curves on rotational CRPC surfaces \mathbf{s} . The principal curvature lines of a rotational surface are its profile curves in planes through the axis (which we identify with the x_3 -axis of a Cartesian system) and its parallel circles (in planes orthogonal to the axis, i.e. $x_3 = \text{const}$). Throughout the paper we assume that κ_1 refers to the normal curvature of the circles and κ_2 to the normal curvature of the profile curves. The Gaussian images of the principal curvature lines of \mathbf{s} are the circles of constant latitude (in planes orthogonal to the x_3 -axis) and constant longitude (in planes through the x_3 -axis) on the unit sphere S^2 . The characteristic curves \mathbf{c} of \mathbf{s} intersect the parallel circles of \mathbf{s} under constant angle γ . Such curves (for any constant angle) are called *loxodromes*. Their Gaussian normal images intersect the circles of constant longitude (or planes through the x_3 -axis) under the constant angle γ (see Fig. 3). These curves are the well-known spherical loxodromes. A spherical loxodrome $\mathbf{n}(u)$, as Gaussian normal image of a characteristic curve $\mathbf{c}(u)$ can be parameterized via the rotational angle u about the x_3 -axis as (see e.g. Wunderlich, 1950),

$$\mathbf{n}(u) = \frac{1}{\cosh qu}(-\sin u, \cos u, \sinh qu), \quad q = \cot \gamma = \sqrt{|\kappa_2/\kappa_1|} = 1/\sqrt{|a|}. \quad (1)$$

Lemma 1. *The Gaussian normal images of the characteristic curves of a rotational CRPC surface are spherical loxodromes and congruent to the curve (1).*

Of course, the γ -loxodromes on any rotational surface form two families of congruent curves. Curves in one family are related to each other by rotation about the axis and the two families are related by a reflection at profile planes. This type of congruence also applies in the following statements.

This forms the basis for our further derivations. Since the characteristic curves may either be asymptotic curves or conjugate and symmetric to principal directions, we have to distinguish these two cases. However, having done the case $a < 0$, it requires only small changes to obtain the rotational CRPC surfaces with $a > 0$.

2.3. The asymptotic curves of negatively curved rotational CRPC surfaces

We would like to determine a characteristic curve $\mathbf{c}(u)$ on a rotational CRPC surface \mathbf{s} with $a < 0$. Since \mathbf{c} is an asymptotic curve, its osculating planes are tangent planes of \mathbf{s} and thus the Darboux frame of \mathbf{s} along \mathbf{c} equals the Frenet frame $\mathbf{e}_1, \mathbf{e}_2, \mathbf{e}_3$ of \mathbf{c} . The binormal vectors \mathbf{e}_3 are the normal vectors \mathbf{n} of \mathbf{s} along \mathbf{c} , represented by the spherical loxodrome (1). The loxodrome may be called the spherical binormal image of \mathbf{c} .

The spherical tangent image $\mathbf{e}_1(u)$ of \mathbf{c} is obtained as follows. We compute the envelope of planes $\mathbf{e}_3(u) \cdot \mathbf{x} = 0$,

$$\mathbf{T}_1(u) : x_1 \sin u - x_2 \cos u - x_3 \sinh qu = 0.$$

These planes are parallel to the osculating planes of \mathbf{c} (tangent planes of \mathbf{s}). Their envelope is a cone Γ_1 with vertex \mathbf{o} through the spherical tangent image $\mathbf{e}_1(u)$. We compute it by intersecting $\mathbf{T}_1(u)$ with the derivative planes $\dot{\mathbf{T}}_1(u)$. The intersection of Γ_1 with the plane $x_3 = 1$ is the curve

$$\mathbf{e}_1^*(u) = (\sinh qu \sin u + q \cosh qu \cos u, -\sinh qu \cos u + q \cosh qu \sin u, 1). \quad (2)$$

Normalization yields the spherical tangent image $\mathbf{e}_1(u) = \mathbf{e}_1^*(u) / \|\mathbf{e}_1^*(u)\|$.

In other words, the curves $\mathbf{e}_3(u)$ and $\mathbf{e}_1(u)$ are related by orthogonality on the spheres S^2 . It is well-known and easily seen that this spherical duality maps a loxodrome $\mathbf{e}_3(u)$ to a *spherical tractrix of the great circle in the plane $x_3 = 0$* with γ as the constant pull distance (see e.g. Wunderlich, 1950; and Fig. 3). We have therefore shown the following result:

Lemma 2. *The tangent images of the asymptotic curves on rotational CRPC surfaces with $a < 0$ are spherical tractrices of a great circle in the plane orthogonal to the rotational axis. Up to rotation about the axis or a reflection at a plane orthogonal to the axis, these curves are represented by $\mathbf{e}_1(u) = \mathbf{e}_1^*(u) / \|\mathbf{e}_1^*(u)\|$ with $\mathbf{e}_1^*(u)$ from equation (2).*

Remark. This result can also be derived directly with help of the Frenet frame as follows (Fig. 3, left). At any point of \mathbf{c} , the tangent vector \mathbf{e}_1 forms a constant angle with the tangent \mathbf{p} of the parallel circle (normal of the profile plane). Note that \mathbf{p} lies in the tangent plane of \mathbf{s} and thus in the osculating plane of \mathbf{c} . Hence, the vector \mathbf{p} is fixed in the moving Frenet frame,

$$\mathbf{p} = \mathbf{e}_1 \cos \gamma + \mathbf{e}_2 \sin \gamma.$$

The Frenet frame vectors describe the spherical tangent image $\mathbf{e}_1(u)$, principal normal image $\mathbf{e}_2(u)$ and binormal image $\mathbf{e}_3(u)$ on S^2 . By the Frenet equations, the tangents $\dot{\mathbf{e}}_1$ and $\dot{\mathbf{e}}_3$ are parallel to \mathbf{e}_2 . In other words, the great circle defined by $\mathbf{e}_1, \mathbf{e}_2$ touches the spherical tangent image $\mathbf{e}_1(u)$ and the great circle in the plane $\mathbf{e}_3, \mathbf{e}_2$ is tangent to the binormal image $\mathbf{e}_3(u)$. The vector \mathbf{p} traces out a great circle c_p in a plane orthogonal to the rotational axis. The constant angle between \mathbf{e}_1 and \mathbf{p} implies that the great circular arc between \mathbf{e}_1 and \mathbf{p} has constant spherical length γ and is tangent at $\mathbf{e}_1(u)$. This reveals the spherical tangent image $\mathbf{e}_1(u)$ as a spherical tractrix of a great circle with γ as the constant pull distance. By the way, our asymptotic curves \mathbf{c} are generalized curves of constant slope in the sense of Pottmann (1982).

We now determine the asymptotic curves \mathbf{c} from the known Frenet frame. Note that the binormals \mathbf{e}_3 agree with the surface normals and lie in the profile planes $P(u) : x_1 \cos u + x_2 \sin u = 0$. Hence, we have to ensure that $\mathbf{c}(u)$ also lies in $P(u)$. Therefore we represent \mathbf{c} as

$$\mathbf{c}(u) = (-r(u) \sin u, r(u) \cos u, h(u)). \quad (3)$$

Of course, the cylinder coordinates $(r(u), h(u))$ are a parameterization of the profile curves of our surfaces \mathbf{s} we look for. The first derivative vectors of \mathbf{c} must be parallel to $\mathbf{e}_1(u)$ or equivalently $\mathbf{e}_1^*(u)$,

$$(-\dot{r} \sin u - r \cos u, \dot{r} \cos u - r \sin u, \dot{h}) = \lambda(u) \mathbf{e}_1^*(u). \quad (4)$$

This yields the following simple differential equations,

$$\frac{\dot{r}}{r} = \frac{1}{q} \tanh qu, \quad \frac{r}{\dot{h}} = -q \cosh qu. \quad (5)$$

For the left one, one finds the solution

$$r = C \cosh^{\frac{1}{q^2}}(qu).$$

As it is sufficient to determine our surfaces up to similarities, we set $C = 1$. Also, we note

$$\frac{1}{q^2} = |a| = -a,$$

and thus in the following write

$$r(u) = \cosh^{-a}(qu), \quad q = 1/\sqrt{|a}|. \quad (6)$$

Thus, we determine the top views of the asymptotic curves via elementary functions. For the third coordinate $h(u)$ we use the right equation in (5) and (6) to obtain

$$h(u) = \pm \frac{1}{q} \int \cosh^{-a-1}(qu) du. \quad (7)$$

The \pm signs are due to the fact that there are two families of asymptotic curves, which are related by a reflection at a horizontal plane. This plane is $x_3 = 0$ if we set the integration constant in (7) so that $h(0) = 0$, and then note the axial symmetry of the asymptotic curve $\mathbf{c}(u)$ with respect to the x_1 -axis ($h(-u) = -h(u)$, $r(-u) = r(u)$).

2.4. Characteristic curves for positive curvature

For a rotational CRPC surface \mathbf{s} with $a > 0$, we consider the developable surface Δ which is tangent to \mathbf{s} along a characteristic curve $\mathbf{c}(u)$. Its rulings are conjugate to the tangents of \mathbf{c} and therefore characteristic directions as well. The surface Δ is the tangent surface of a space curve $\mathbf{d}(u)$, the so-called regression curve of Δ . The tangent planes along rulings of Δ are the osculating planes of \mathbf{d} . Hence, the binormal image of \mathbf{d} is the normal image $\mathbf{n}(u)$, the tangent image of \mathbf{d} is a spherical tractrix and the tangents of \mathbf{d} are parallel to the vectors $\mathbf{e}_1^*(u)$ in (2). Characteristic directions are symmetric with respect to the principal directions, and thus the tangent vectors of the curve $\mathbf{d}(u)$ are obtained from those of $\mathbf{c}(u)$ by reflection at the corresponding tangent $(\cos u, \sin u, 0)$ of the parallel circle. This shows that the tangent vectors $\mathbf{e}_1(u)$ of $\mathbf{c}(u)$ are parallel to

$$\bar{\mathbf{e}}_1(u) = (-\sinh qu \sin u + q \cosh qu \cos u, \sinh qu \cos u + q \cosh qu \sin u, -1). \quad (8)$$

Geometrically, one may express this as follows (indicated in Fig. 3, left):

Lemma 3. *The tangent images of the characteristic curves on rotational CRPC surfaces with $a > 0$ are obtained by spherically reflecting the points of a spherical tractrix of a great circle at the corresponding points of this great circle. Up to rotation about the axis, these curves are represented by $\mathbf{e}_1(u) = \bar{\mathbf{e}}_1(u)/\|\bar{\mathbf{e}}_1(u)\|$ with $\bar{\mathbf{e}}_1(u)$ from equation (8).*

Remark. Now, the regression curves \mathbf{d} of the tangent developables along the characteristic curves \mathbf{c} are generalized curves of constant slope (Pottmann, 1982).

As before, we represent the characteristic curve in the form (3) and make sure that its first derivative is parallel to $\bar{\mathbf{e}}_1(u)$ in (8). Hence, we have to replace \mathbf{e}_1^* by $\bar{\mathbf{e}}_1$ in equation (4) and find the differential equations

$$\frac{\dot{r}}{r} = -\frac{1}{q} \tanh qu, \quad \frac{r}{h} = q \cosh qu. \quad (9)$$

With $-\frac{1}{q^2} = -a$, this results again in

$$r(u) = \cosh^{-a}(qu), \quad h(u) = \pm \frac{1}{q} \int \cosh^{-a-1}(qu) du.$$

Let us summarize our results:

Theorem 1. *The rotational surfaces with $\kappa_1/\kappa_2 = a$ are parameterized as*

$$\mathbf{s}(u, v) = (r(u) \cos v, r(u) \sin v, h(u)), \quad (10)$$

where the profile curve representation $((r(u), h(u)))$ is given by equations (6) and (7). Their characteristic curves $u \pm v = C$ have top views with an elementary polar coordinate representation (6).

From our parameterization of the profile curves, it is easy to obtain their known graph representation $h(r)$. Using

$$\frac{dh}{dr} = \frac{\dot{h}}{\dot{r}} = \frac{\pm 1}{\sinh(qu)} = \frac{\pm 1}{\sqrt{\cosh^2(qu) - 1}} = \frac{\pm r^{1/a}}{\sqrt{1 - r^{2/a}}},$$

we find

$$h(r) = \pm \int \frac{r^{1/a}}{\sqrt{1 - r^{2/a}}} dr. \quad (11)$$

There is a simple direct derivation of this form due to Hopf (1951), described nicely in Kühnel (2013), Ex. 3.27.

It is well-known (see e.g. Strubecker, 1969, pp. 162) that a rotational surface given in the form (10) can be mapped conformally to an (X, Y) -plane via

$$(X, Y) = (v, \int \frac{\sqrt{\dot{r}(u)^2 + h(u)^2}}{r(u)} du).$$

For our surfaces, this conformal image is

$$(X, Y) = (v, u \tan \gamma). \quad (12)$$

Parallel circles and profile curves are mapped to lines parallel to the X -axis and Y -axis, respectively. Loxodromes of \mathbf{s} with a constant angle ω against the parallel circles are mapped to straight lines with slope $\tan \omega$, and therefore expressed as

$$u \tan \gamma = v \tan \omega.$$

For $\omega = \gamma$ this shows again that the curves $u = v$ are γ -loxodromes. As is true for any rotational surface, the loxodromes to different angles are related to each other by axial fan transformations, in cylinder coordinates expressed by $(r, v, h) \mapsto (r, bv, h)$ with constant b .

We also see that the parameter change $\bar{u} := u \tan \gamma$ yields an *isothermic parameterization* $\mathbf{s}(\bar{u}, v)$ of the rotational CRPC surfaces.

2.5. Pairs of surfaces with the same absolute value of the principal curvature ratio

It turns out that there is a remarkably simple relation between two rotational CRPC surfaces which belong to principal curvature ratios $\pm a$. It becomes most easily accessed if we turn to a characteristic parameterization $\mathbf{S}(U, V)$, where the curves $U = \text{const}$ and $V = \text{const}$ are the characteristic curves.

Noting that in the current representation $\mathbf{s}(u, v)$, the preimages of the characteristic curves in the parameter plane are the lines $u = C \pm v$, we see that a characteristic parameterization is achieved via the parameter change $u = U - V, v = U + V$,

$$\mathbf{S}(U, V) = \mathbf{s}(U - V, U + V).$$

This implies

$$\begin{aligned} \mathbf{S}_U &= \mathbf{s}_u + \mathbf{s}_v = (\dot{r} \cos v - r \sin v, \dot{r} \sin v + r \cos v, \dot{h}), \\ \mathbf{S}_V &= -\mathbf{s}_u + \mathbf{s}_v = (-\dot{r} \cos v - r \sin v, -\dot{r} \sin v + r \cos v, -\dot{h}). \end{aligned}$$

We consider now a surface $\mathbf{S}(u, v)$ to the constant a and the surface $\bar{\mathbf{S}}(u, v)$ to $-a$. In view of equations (5) and (9), the corresponding functions r and h are related by

$$\frac{\dot{\bar{r}}}{\bar{r}} = -\frac{\dot{r}}{r}, \quad \frac{\bar{r}}{\bar{h}} = -\frac{r}{h},$$

which yields

$$\bar{\mathbf{S}}_U = \frac{\bar{r}}{r} \mathbf{S}_V, \quad \bar{\mathbf{S}}_V = \frac{\bar{r}}{r} \mathbf{S}_U. \quad (13)$$

These relations characterize the two parameterizations as *reciprocal parallel* (see Sauer, 1970, pp. 177). They show that the two surfaces may be seen as *membranes in equilibrium and as reciprocal force diagrams of each other* (Sauer, 1970, pp. 225), which will become more intuitive at hand of the discrete versions in Section 3.4.1.

This mechanical interpretation is closely related to the following one, which relies on *relative differential geometry*, introduced by Müller (1921). One replaces the Euclidean sphere by another surface Σ , usually one with positive curvature, but this is not necessary. Then, the Gauss map from a surface \mathbf{S} to the relative sphere Σ is defined via parallel oriented tangent planes, and relative principal curvatures κ_1^r, κ_2^r are the eigenvalues of the (negative) derivative σ^r of this map. As long as one of the two corresponding points of \mathbf{S} and Σ is elliptic ($K > 0$), there are two real eigenvalues. Obviously curvatures do not change if one applies the same affine map to \mathbf{S} and Σ . Relative minimal surfaces, studied by Müller (1921), are defined by $2H^r = \kappa_1^r + \kappa_2^r = 0$.

Points of \mathbf{S} and $\bar{\mathbf{S}}$ to the same (U, V) have parallel tangent planes, seen e.g. in equation (13), and thus correspond to each other in the relative Gauss map σ^r if we view one of them, e.g. \mathbf{S} with $a > 0$, as relative sphere. The eigenvectors of σ^r (relative principal curvature directions) are the Euclidean principal curvature directions. With the Euclidean shape operators σ and $\bar{\sigma}$, the relative shape operator is $\sigma^r = \sigma^{-1} \circ \bar{\sigma}$, whose trace vanishes, and thus $H^r = 0$. We have proved the following result:

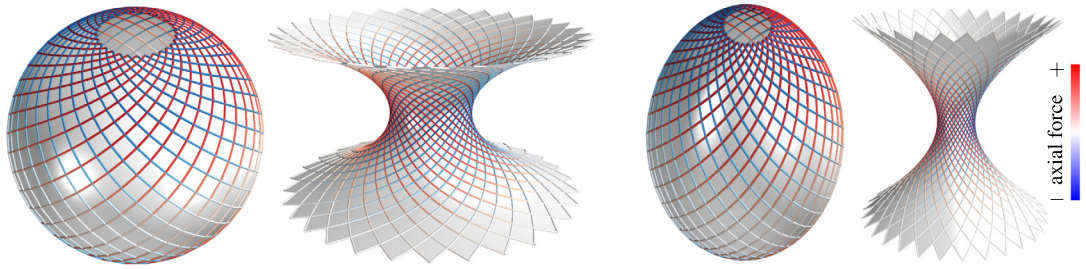


Fig. 4. Pairs of rotational CRPC surfaces with the same value of $|a|$. Forces (color) can be assigned to characteristic nets so that such pairs are reciprocal force diagrams of surfaces in equilibrium. Left two: Orthogonal system of spherical loxodromes ($a = 1$), which is a material minimizing structure according to Michell, and the reciprocal force diagram aligned with the asymptotic curves on a catenoid ($a = -1$). Right two: Pair of rotational CRPC surfaces with $a = \pm 3$, with forces in the interpretation as reciprocal diagrams.

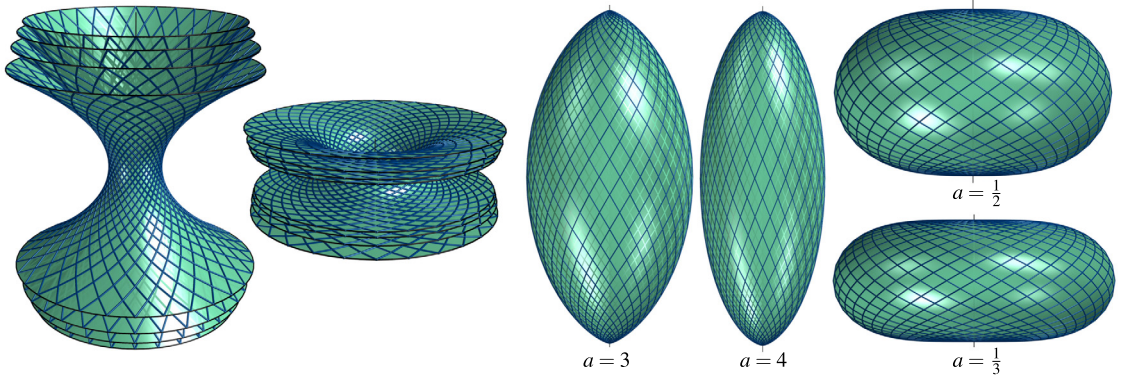


Fig. 5. Rotational CRPC surfaces. Left: $a = -2, -3, -4, -5$ and $a = -\frac{1}{5}, -\frac{1}{4}, -\frac{1}{3}, -\frac{1}{2}$ from outside to inside. Right: $a = 3, 4, \frac{1}{2}, \frac{1}{3}$.

Theorem 2. Two rotational surfaces \mathbf{S} with $\kappa_1/\kappa_2 = a$ and $\bar{\mathbf{S}}$ with $\kappa_1/\kappa_2 = -a$ and parallel axes are reciprocal force diagrams of each other (in their characteristic parameterization) and they form a pair of relative minimal surfaces.

Remark. Numerical tests on discrete models (Section 3) indicate that a similar result does not hold for general CRPC surfaces. C-nets of CRPC surfaces to $a < 0$ are A-nets and as such can be brought into equilibrium. There is a family of possible reciprocal force diagrams which are related by Combescure transformations (Sauer, 1970). The corresponding nets on the reciprocal surfaces are conjugate and isogonal, but in general not principal symmetric. For rotational CRPC surfaces principal symmetry follows from rotational symmetry (see also Section 3.4.1). Another case where we get principal symmetry for the reciprocal nets is that of minimal surfaces ($a = -1$). They possess reciprocal orthogonal Q-nets. These are principal nets and Combescure transforms of their common Gaussian spherical image. This yields the well-known reciprocal pairs formed by an A-net on a minimal surface and an orthogonal spherical net.

2.6. Examples

$a = \pm 1$: The simplest examples of rotational CRPC surfaces are the ones when $a = \pm 1$, i.e., $q = 1$. Their characteristic curves intersect under a right angle. The case $a = 1$ characterizes a surface with only umbilics and thus a sphere. Indeed, we obtain $r = 1/\cosh u, h = \tanh u$, which is a spherical loxodrome (1) to $q = 1$. The associated surface $a = -1$ must be a Euclidean rotational minimal surface, i.e. a catenoid: we find $r = \cosh u, h = -u$, and thus the profile is the known catenary $r = \cosh h$. This is also in accordance with Theorem 2. The mechanical interpretation of minimal surfaces and spheres as reciprocal force diagrams is due to W. Blaschke (see Blaschke, 1930, pp.244). The equilibrium configuration of orthogonal spherical loxodromes also appears as a material minimizing form in the seminal paper by Michell (1904) (see Fig. 4, left).

$a = -2$: With $r(u) = \cosh^2(u/\sqrt{2}), h(u) = \pm 2 \sinh(u/\sqrt{2})$, we obtain $4r - h^2 = 4$ for the profile. Hence, it is a parabola with its directrix as the rotational axis. The resulting rotational surface is of algebraic degree four.

While at first sight this is a bit surprising, it is just a direct consequence of a well-known construction of the curvature centers of a parabola, illustrated in Fig. 6. One has to note that the principal curvature centers of a rotational surface at a point \mathbf{p} are the curvature center \mathbf{f}_1 of the profile curve at \mathbf{p} and the intersection point \mathbf{f}_2 of the normal at \mathbf{p} with the rotational axis.

$a = 3$: $\gamma = \pi/3, r(u) = \cosh^{-3}(u/\sqrt{3}), h(u) = \pm(3 \tanh(u/\sqrt{3}) - \tanh^3(u/\sqrt{3}))$. This profile curve $(r(u), h(u))$ is a well-known rational algebraic curve of order 6 and class 4, namely a special involute of an astroid (see Fig. 7). To verify its

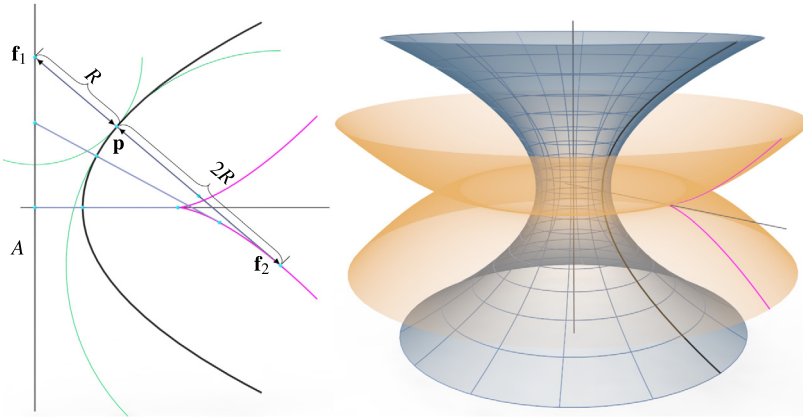


Fig. 6. A well-known construction of the curvature centers f_2 of a parabola (left) from the intersection points f_1 of its normals with the directrix A shows that the surface obtained by rotating a parabola about its directrix A has a constant negative ratio of principal curvatures $\kappa_1/\kappa_2 = -2$. We also show the evolute of the parabola, which generates the nontrivial part of the focal surface of the CRPC surface.

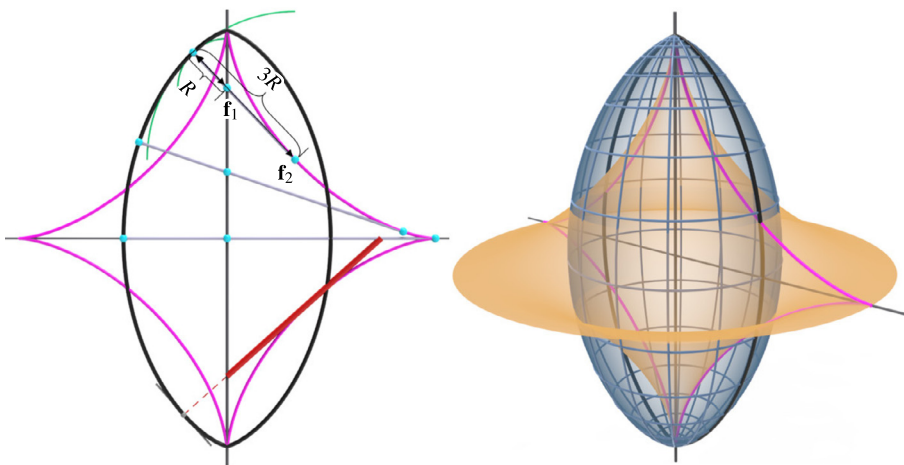


Fig. 7. The evolute of the profile of a rotational CRPC surface to $a=3$ is an astroid. The CRPC surface is algebraic of order 6 and has two singular points on the rotational axis. We find this behavior at points of the rotational axis (umbilic with curvature radius 0) for all rotational CRPC surfaces with $a > 1$.

evolute as an astroid, we compute the intersection points of its tangents with the coordinate axes and find the two points $(2 \cosh^{-1}(u/\sqrt{3}), 0)$ and $(0, -2 \tanh(u/\sqrt{3}))$, whose distance equals 2 for all u . Hence, the evolute is the envelope of a straight line segment of constant length (red in Fig. 7, left) whose endpoints run on two orthogonal lines. This curve is called astroid and has another kinematic generation as path of a point on a circle of diameter 1 which rolls inside a circle of radius 2. Since one of the involutes of an astroid is again an astroid, our profile is also an offset of that astroid.

For more examples, in particular higher order algebraic ones, we refer to recent work by Jimenez (2021).

3. Discrete CRPC surfaces

In this section, we study discrete CRPC surfaces based on their characteristic nets. The simple discrete models enable an efficient computation and the development of computational tools to explore the shape space of CRPC surfaces.

Our discretization largely follows prior work on special discrete parameterizations (nets). These are the very well studied asymptotic nets (A-nets) and conjugate nets (Q-nets) (Bobenko and Suris, 2008) and the recently introduced principal symmetric nets (Pellis et al., 2020). We describe three different discretizations of the constant angle and also present a simple way to compute discrete surfaces which are invariant under uniform motions in the group of similarities (rotational, helical and spiral surfaces). A comparison of discrete rotational CRPC surfaces with their smooth counterparts reveals the high quality of the discrete models. Moreover, these special CRPC surfaces as well as discrete minimal surfaces are suitable starting nets for exploring possible shapes of CRPC surfaces.

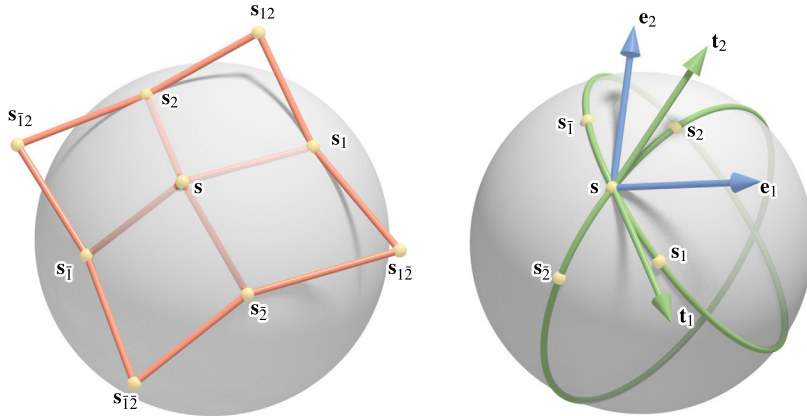


Fig. 8. *Left:* In an S-net, any central vertex s and its four neighbors $s_1, s_2, \bar{s}_1, \bar{s}_2$ lie on a common sphere. *Right:* Discrete osculating circles of the two discrete parameter lines through a vertex. The bisecting vectors e_1, e_2 of their tangent vectors t_1, t_2 are the discrete principal directions (images from Pellis et al., 2020).

3.1. Discrete C-nets

Characteristic nets are regular away from umbilics (including those with curvature 0 and ∞). They are discretized as quad meshes which have regular combinatorics (inner vertices of valence 4), apart from isolated combinatorial singularities (inner vertices with valence $\neq 4$).

In the following, we restrict to regular discrete nets defined by a map $\mathbf{s} : \mathbb{Z}^2 \rightarrow \mathbb{R}^3$. The discrete parameter lines through $(u, v) \in \mathbb{Z}^2$ are polylines $\mathbf{s}(\mathbb{Z}, v)$ and $\mathbf{s}(u, \mathbb{Z})$ which we call u -lines and v -lines like in the smooth case.

When considering local properties of a net around $\mathbf{s}(u, v)$, we use the shift notation as in Bobenko and Suris (2008) (Fig. 8, left):

$$\begin{aligned} \mathbf{s} &= \mathbf{s}(u, v), & \mathbf{s}_1 &= \mathbf{s}(u+1, v), & \mathbf{s}_2 &= \mathbf{s}(u, v+1), \\ \mathbf{s}_{\bar{1}} &= \mathbf{s}(u-1, v), & \mathbf{s}_{\bar{2}} &= \mathbf{s}(u, v-1), & \mathbf{s}_{12} &= \mathbf{s}(u+1, v+1). \end{aligned}$$

Asymptotic nets. In the negatively curved case, characteristic nets (C-nets) are asymptotic nets (A-nets). These are quad nets in which all regular vertices have *planar vertex stars*. This means that the five points $\mathbf{s}, \mathbf{s}_1, \mathbf{s}_2, \mathbf{s}_{\bar{1}}, \mathbf{s}_{\bar{2}}$ lie in a plane. This plane is identical with the discrete osculating planes ($\mathbf{s}_1 \mathbf{s} \mathbf{s}_2$) and ($\mathbf{s}_{\bar{2}} \mathbf{s} \mathbf{s}_1$) of the two discrete parameter lines passing through a vertex \mathbf{s} and it is also the discrete tangent plane at \mathbf{s} . This expresses the asymptotic property, since an asymptotic curve of a smooth surface is one whose osculating planes are tangent to the surface.

Conjugate and principal symmetric nets. In the positively curved case, a C-net is conjugate and principal symmetric. Conjugate nets (Q-nets) are characterized by *planar faces* ($\mathbf{s} \mathbf{s}_1 \mathbf{s}_2 \mathbf{s}_{12}$) (Bobenko and Suris, 2008). Principal symmetry can be expressed in two ways (Pellis et al., 2020): one approach (S-nets) is vertex-based and a concept of Möbius sphere geometry and the other one is face-based (S^* -nets) and a concept of Laguerre sphere geometry.

S-nets. Here, *each vertex star is spherical*, i.e., a regular vertex and its 4 connected neighbors $\mathbf{s}, \mathbf{s}_1, \mathbf{s}_2, \mathbf{s}_{\bar{1}}, \mathbf{s}_{\bar{2}}$ lie on a common sphere (Fig. 8, left). This sphere expresses principal symmetry of the parameter lines for the following reason: The discrete osculating circles of the parameter lines pass through $\mathbf{s}_1 \mathbf{s} \mathbf{s}_2$ and $\mathbf{s}_{\bar{2}} \mathbf{s} \mathbf{s}_1$, respectively (Fig. 8, right) and lie on the sphere associated to the vertex. As a sphere tangent to the discrete surface at \mathbf{s} and containing the osculating circles, it is the common discrete Meusnier sphere of the two parameter lines. Hence, the two parameter lines have the same discrete normal curvature $\kappa_n = 1/r$, with r as radius of the sphere. Thus, the discrete tangents $\mathbf{t}_1, \mathbf{t}_2$ of the parameter lines at \mathbf{s} (tangents of the circles) are symmetric to the discrete principal directions e_1, e_2 . Those arise now naturally as the bisectors of $\mathbf{t}_1, \mathbf{t}_2$.

Note that A-nets are principal symmetric as well and appear now as limits of S-nets in which the vertex spheres have radius ∞ , i.e. are planes. We obtain normal curvature $\kappa_n = 0$ for the parameter lines which are therefore asymptotic curves.

3.2. Discrete CRPC surfaces as discrete isogonal C-nets

Having a simple discretization of C-nets at our disposal, we arrive at discrete CRPC surfaces by expressing a constant angle 2γ between parameter lines. The targeted constant principal curvature ratio is taken from the smooth case as $\gamma = \arctan \sqrt{|\kappa_1/\kappa_2|}$.

The definition of discrete angles can happen in various ways which we would like to describe now.

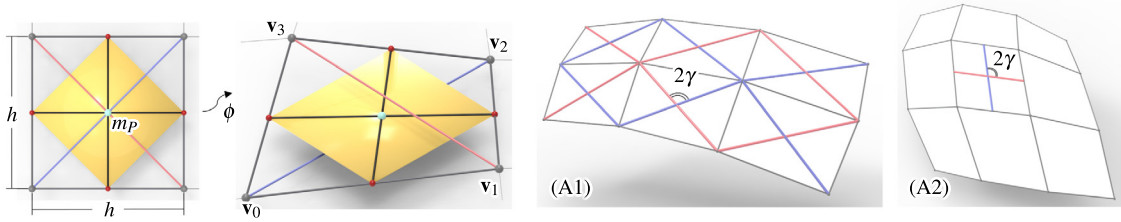


Fig. 9. Left: If the vertices of a face in a quad mesh are viewed as image of a square in the parameter plane under a smooth map ϕ , central parallelograms (yellow) define an affine map, which approximates the derivative of ϕ at the center m_P with order $O(h^2)$. This results in two simple ways of measuring angles between discrete parameter lines in quad meshes. Angle measurement (A1): Given a quad mesh (black), called control mesh, its face diagonals can be arranged in two quad meshes (red, blue). Angles between parameter lines in these diagonal meshes are defined as angles between the two diagonals in each quad of the control mesh. Angle measurement (A2): Intersection angles between parameter lines in a quad net can also be measured between the central lines in each face of the net.

Angles between osculating circles. As illustrated in Fig. 8, right, we can define the angle 2γ as the angle between tangents $\mathbf{t}_1, \mathbf{t}_2$ to the discrete osculating circles at a vertex s . This method also works for A-nets and has been applied in Pellis et al. (2020), where one finds the details for formulating the angle constraint. It has the advantage of being invariant under Möbius transformations. Note that Möbius transformations map S-nets to S-nets, circles to circles, and they preserve angles between curves. Hence, this method is attractive when studying isogonal S-nets. However, our focus is on isogonal C-nets which are not invariant under Möbius transformations. Moreover, there are computationally simpler ways for angle measurement in discrete nets, which we will now describe (see Fig. 9) and which are used in our results.

These methods are based on the following fact (Fig. 9): We view vertices of a quad mesh as images of the standard lattice $h\mathbb{Z}^2$ with stepsize h under a smooth mapping ϕ to \mathbb{R}^3 . Then, a face $F = (\mathbf{v}_0, \dots, \mathbf{v}_3)$ of the quad mesh corresponds to a square P in the (u, v) parameter plane. The edge midpoints of F form a parallelogram F_m whose edges are parallel to the diagonals of the quad. This is an immediate consequence of the intercept theorem and sometimes called Varignon's theorem. Edge midpoints of the corresponding square in the parameter plane form a square P_m . The unique affine map $P_m \rightarrow F_m$ is an approximation of the derivative map of ϕ , evaluated at the center m_P of P , with approximation error $O(h^2)$. This follows from a Taylor expansion of ϕ at m_P (Jiang et al., 2021a). Hence, the partial derivatives of ϕ are approximated via the central lines of F (diagonals of F_m), as

$$\phi_u(m_P) = \frac{1}{2h}(\mathbf{v}_1 + \mathbf{v}_2 - \mathbf{v}_0 - \mathbf{v}_3) + O(h^2), \quad \phi_v(m_P) = \frac{1}{2h}(\mathbf{v}_2 + \mathbf{v}_3 - \mathbf{v}_0 - \mathbf{v}_1) + O(h^2).$$

Likewise, the edge vectors of F_m (diagonal vectors of F) approximate derivatives of ϕ in diagonal direction, which has been used in recent work (Jiang et al., 2020, 2021b,a) and leads to our first approach:

Angles via diagonal meshes (Fig. 9, A1). One starts with a quad mesh, called *control net* that needs not fulfill the constraints of the specific discretization one has in mind. The actual targeted nets are the two *diagonal nets* of the control net and the constraints (in our case of a C-net) are applied to both of them. The angle between parameter lines is measured in each face of the control mesh as the angle between diagonals. Expressing a constant angle and having both diagonal nets as C-nets yields discrete CRPC surfaces.

Angles via central lines in quad faces (Fig. 9, A2). The diagonal mesh approach has the slight disadvantage that one designs a pair of meshes (diagonal meshes) which are subject to the same constraints, but only one mesh may be needed. In the following, we think of a single quad mesh which is our targeted net to which the constraints are applied. Angles between parameter lines are now measured between the central lines in a face.

Remark. The latter type of angle measurement for discrete nets has not yet been explored in discrete differential geometry, and it is not clear where it provides benefits in the discrete theory. So far, discrete orthogonal nets have been studied mostly for Q-nets, which leads to principal nets (Bobenko and Suris, 2008). Discrete orthogonality away from principal parameterizations has been addressed at a few places, e.g. for discrete orthogonal geodesic nets (representing discrete developable surfaces) (Rabinovich et al., 2018), or their generalizations to discrete geodesic parallel coordinates (Wang et al., 2019). Note that right angles between central lines of a quad are equivalent to diagonals of equal length in that quad, since edge midpoints form the vertices of a rhombus whose edges have half the length of the diagonals in the quad.

A comparison of the three types of angle measurement is provided in Fig. 10.

3.3. Constraint formulation and numerical optimization

The proposed discrete CRPC surfaces are constrained quad meshes and thus can be computed by known efficient numerical optimization algorithms. We follow the approach of Tang et al. (2014). There, one tries to get along with constraints

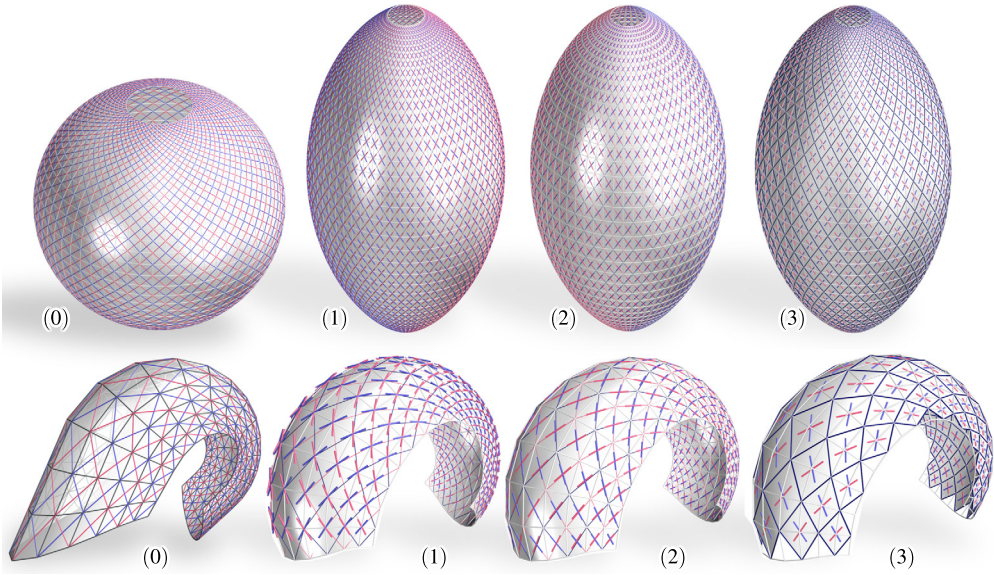


Fig. 10. All three types of angle measurement (1,2,3) lead to very similar results when optimization for a CRPC surface is applied on an initial shape (0), here represented by two diagonal meshes of a control mesh. Angles between discrete osculating circles are enforced on both diagonal meshes (1) and angles between diagonals in faces of the control mesh are applied in (2) and the blue diagonal mesh is optimized with angles between central lines in faces (3). Top row: Starting from a sphere, we optimize for a rotational CRPC surface with $a = 3$. Bottom row: An initial mesh, not representing a CRPC surface, is optimized for a CRPC surface with $a = 0.45$.

that are at most quadratic, even if one has to use auxiliary variables. Constraint solving is based on a nonlinear least squares formulation, and optimization is performed with a Levenberg–Marquardt algorithm.

We now show how the various constraints are formulated and point out that in the diagonal net approach the relevant constraints have to be applied to both diagonal nets.

A-nets. Planar regular vertex stars are achieved by introduction of unit vertex normals \mathbf{n} as additional variables and expressing orthogonality to the 4 emanating edges,

$$\mathbf{n}^2 = 1, \quad \mathbf{n} \cdot (\mathbf{s}_j - \mathbf{s}) = 0, \quad j \in \{1, \bar{1}, 2, \bar{2}\}. \quad (14)$$

S-nets. Spherical regular vertex stars are obtained by adding a sphere center \mathbf{c} as an additional variable at each vertex \mathbf{s} , and expressing equal distance of \mathbf{c} to the 5 vertices of a vertex star. This means $\|\mathbf{s} - \mathbf{c}\|^2 = \|\mathbf{s}_j - \mathbf{c}\|^2$, or

$$\mathbf{s}^2 - \mathbf{s}_j^2 + 2(\mathbf{s}_j - \mathbf{s}) \cdot \mathbf{c} = 0 \quad j \in \{1, \bar{1}, 2, \bar{2}\}. \quad (15)$$

In general it is good to prepare for cases where sphere centers of an S-net can tend to infinity (see Pellis et al., 2020). However, we are only dealing with S-nets that are also Q-nets. Those cannot be close to A-nets in some regions, because A-nets are not conjugate (asymptotic directions are self-conjugate). The only places in which the spheres may get an infinite radius are at discrete flat points which are combinatorial singularities of the net and not subject to the constraints above.

Q-nets. Planarity of a face ($\mathbf{s}_1 \mathbf{s}_{12} \mathbf{s}_2$) is expressed with help of an additional face normal vector \mathbf{n}_f via orthogonality to each edge of the face,

$$\mathbf{n}_f^2 = 1, \quad \mathbf{n}_f \cdot (\mathbf{s}_1 - \mathbf{s}) = 0, \quad \mathbf{n}_f \cdot (\mathbf{s}_{12} - \mathbf{s}_1) = 0, \quad \mathbf{n}_f \cdot (\mathbf{s}_2 - \mathbf{s}_{12}) = 0, \quad \mathbf{n}_f \cdot (\mathbf{s}_2 - \mathbf{s}) = 0. \quad (16)$$

While three orthogonality constraints would be sufficient, the use of four is more symmetric and easier to implement. Dependent constraints pose no problems to our numerical solver.

Constant angle. If $\mathbf{v}_a \mathbf{v}_b \mathbf{v}_c \mathbf{v}_d$ is a quad face of the control mesh, the angle constraint based on the use of two diagonal meshes is

$$\frac{\mathbf{v}_c - \mathbf{v}_a}{\|\mathbf{v}_c - \mathbf{v}_a\|} \cdot \frac{\mathbf{v}_d - \mathbf{v}_b}{\|\mathbf{v}_d - \mathbf{v}_b\|} = \cos 2\gamma. \quad (17)$$

The diagonal lengths $l_1 = \|\mathbf{v}_c - \mathbf{v}_a\|$ and $l_2 = \|\mathbf{v}_d - \mathbf{v}_b\|$ can be separate variables, constrained via additional variables $\mathbf{g}_1, \mathbf{g}_2$ and dummy variables δ_i (to achieve $l_i > 0$) through the quadratic constraints

$$\mathbf{v}_c - \mathbf{v}_a = l_1 \mathbf{g}_1, \mathbf{v}_d - \mathbf{v}_b = l_2 \mathbf{g}_2, \quad \mathbf{g}_i^2 = 1, \quad l_i = \delta_i^2, \quad i = 1, 2.$$

Then the angle constraint $(\mathbf{v}_c - \mathbf{v}_a) \cdot (\mathbf{v}_d - \mathbf{v}_b) = l_1 l_2 \cos 2\gamma$ is quadratic. Since we use an iterative algorithm, it is sufficient to take l_i from the previous iteration and avoid these complications.

If we use central lines in the quads of a net for angle discretization, we apply equation (17) to the faces $(\mathbf{s}_1 \mathbf{s}_2 \mathbf{s}_{12})$ and take the points \mathbf{v} as edge midpoints,

$$2\mathbf{v}_a = \mathbf{s} + \mathbf{s}_1, \quad 2\mathbf{v}_b = \mathbf{s}_1 + \mathbf{s}_{12}, \quad 2\mathbf{v}_c = \mathbf{s}_{12} + \mathbf{s}_2, \quad 2\mathbf{v}_d = \mathbf{s}_2 + \mathbf{s}.$$

To achieve an angle $2\gamma \neq \pi/2$ between two straight lines, we have to say where we should have 2γ and where $\pi - 2\gamma$. For that, we select one direction (diagonal vector or central vector) in each face consistently over the mesh in a fair manner and measure angles in a consistent orientation to the other diagonal or central vector. This requires an even valence for all inner vertices, which occurs naturally since the singularities arise from underlying principal nets. For details we refer to Jiang et al. (2020); Jimenez et al. (2020).

Summary of constraints. CRPC surfaces with negative curvature $a < 0$ are subject to the A-net constraints (14) and the chosen angle constraint, while for $a > 0$ they are subject to S-net constraints (15), Q-net constraints (16) and angle constraints. Angles via osculating circles or central lines in quad faces work without additional structure. Angles via diagonal meshes require as additional structure a control mesh (to which none of the constraints is applied) and the two diagonal meshes, to which constraints are applied; angles are measured between the two diagonals in each face of the control mesh. We will later add constraints that yield helical or spiral CRPC surfaces and constraints in connection with user editing as a tool for design space exploration.

Fairness. Having formulated all constraints, we are not yet ready to set up the objective function of optimization, since we have to make sure that we have a discrete model of a smooth surface. This is done by a fairness energy applied to the discrete parameter lines of the nets under consideration. For any three consecutive vertices $\mathbf{v}_i, \mathbf{v}_j, \mathbf{v}_k$ of a polyline that should be fair (typically $\mathbf{s}_1, \mathbf{s}, \mathbf{s}_1$ and $\mathbf{s}_2, \mathbf{s}, \mathbf{s}_2$, but also consecutive vertices of a parameter line in the control mesh of the diagonal mesh approach), the term $(\mathbf{v}_i - 2\mathbf{v}_j + \mathbf{v}_k)^2$ is added to the regularizing part of the objective function. Hence, the regularizing part E_{reg} is just this sum of squared second differences.

Final objective function. The objective function for discrete CRPC surfaces is composed as follows. We consider a vector $X \in \mathbb{R}^d$ that contains all d variables, including the auxiliary ones. Then, each constraint is written in the form $C_i(X) = 0$ and the objective function reads

$$F(X) = \sum C_i(X)^2 + \mu E_{reg}(X) + \varepsilon (X - X^c)^2, \quad (18)$$

where X^c is the current value of X in the iterative procedure. This nonlinear least squares problem is solved with the Gauss-Newton method, which due to the regularizing third part is a Levenberg-Marquardt algorithm. However, the small weight μ of the fairness part fades away in later iterations. The main reason is that this is the only part which does not have a zero residual for the final mesh and its presence may act against a better accuracy for the other essential constraints. Moreover, Gauss-Newton algorithms have local quadratic convergence for zero residual problems, which one does not want to destroy. The small weight ε of the other regularizer does not fade away and ensures a regular linear system even in presence of conflicting constraints or an insufficient number of them, which means design freedom in applications. Details on the choice of weights and on the performance of optimization are provided in subsection 4.2.

Initialization. Since we have here a nonlinear non-convex optimization problem, the success of numerical optimization also depends on a reasonable initialization. For that, we already have some good options: We can start with the parameterization (10) of a rotational CRPC surface, and extract a discrete characteristic net by sampling the parameter plane at an axis-aligned square grid and taking a diagonal net of that grid (then aligned with lines $u \pm v = C$). Using the diagonal mesh approach for angle measurement, sampling at an axis-aligned grid yields a great choice of the control mesh, since then the diagonal meshes will follow characteristic lines. We will see later that this sampling of the smooth solution fulfills our constraints on discrete CRPC nets really well. Starting from rotational shapes, we may cut them open and then gradually move away from rotational shapes. In the following subsection, we show how to obtain helical and spiral CRPC surfaces, and from those we can apply more general editing operations to explore the space of possible shapes (see section 4.3).

During optimization, we may also change the parameter a gradually (not crossing $a = 0$). This leads to a way for constructing negatively curved CRPC surfaces from known orthogonal A-nets representing minimal surfaces ($a = -1$) and positively curved CRPC surfaces from orthogonal spherical nets ($a = 1$). However, in the latter case combinatorial singularities are likely to pose problems. More details are provided in section 4.3.

3.4. Discrete rotational, helical and spiral surfaces

CRPC surfaces are objects of Euclidean similarity geometry. Here a similarity is defined as composition of a rigid body motion and uniform scaling with factor $\sigma \neq 0$; it is represented by $\mathbf{x} \mapsto \sigma A \cdot \mathbf{x} + \mathbf{a}$ with an orthogonal matrix A . Thus it is natural to look at those CRPC surfaces which are invariant under a one-parameter group of Euclidean similarities.

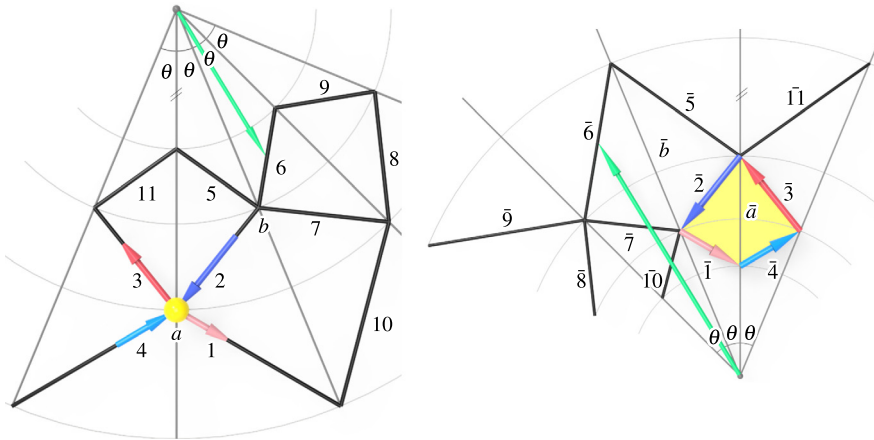


Fig. 11. Radially symmetric nets as reciprocal force diagrams.

Minimal surfaces of that type have been studied (see e.g. Wunderlich, 1952, 1954), but for CRPC surfaces we so far only know rotational surfaces. Results on helical and spiral CRPC surfaces are missing. Hence, we will now show how to compute discrete models of those and we will use them later as initial shapes for the computation of more general CRPC surfaces.

Discrete CRPC surfaces are constrained meshes, for which we now have to add the constraint of being a discrete helical or spiral surface. Hence, we take an arbitrary quad net and derive constraints which make them discrete helical or spiral nets. It is easy to get discrete models by including the helical and spiral paths in the representation, but this is not helpful here, since we require characteristic parameterizations to express the CRPC property.

We use an approach which has been successful in the reconstruction of rotational, helical and spiral surfaces from point clouds (Pottmann and Wallner, 2001; Hofer et al., 2005). There one estimates surface normals and characterizes these special surfaces through velocity vector fields of the motions under consideration which are orthogonal to the normals, i.e., tangential to the surface. Equivalently, this requires the normals to lie in a so-called linear complex of straight lines (helical surface) or line elements (spiral surfaces). Adapting this approach in the present setting is natural since we have well-defined discrete surface normals at vertices of C-nets (normal to the sphere or plane passing through a vertex star).

3.4.1. Discrete rotational CRPC surfaces in force equilibrium

Before moving to helical and spiral surfaces, let us briefly address discrete rotational CRPC surfaces. This illustrates the previous general discretizations and provides a completely elementary approach to Theorem 2.

Let us recall a basic concept of graphic statics. We consider a mesh and want to assign forces to edges so that we obtain a system in equilibrium (see Fig. 11). Each edge with endpoints $\mathbf{v}_i, \mathbf{v}_j$ is assigned a scalar w_{ij} , with the understanding that force $w_{ij}(\mathbf{v}_i - \mathbf{v}_j)$ is exerted on \mathbf{v}_i and the opposite force $w_{ij}(\mathbf{v}_j - \mathbf{v}_i)$ is exerted on \mathbf{v}_j . Equilibrium requires that in the entire mesh the forces acting at each vertex sum to zero. Hence, the forces exerted at a vertex (e.g. the yellow one in Fig. 11, left) are also the edge vectors of a closed polygon (yellow in Fig. 11, right). Those closed polygons form the so-called reciprocal force diagram. Geometrically, the original mesh, called form diagram, and the reciprocal force diagram are two combinatorially dual meshes where corresponding edges are parallel. One speaks of *reciprocal parallel meshes* (Sauer, 1970). The relation between the two diagrams is symmetric: one is a force diagram for the other.

To apply this to our problem, we first consider a planar rotational symmetric net as in Fig. 11, left, and show that there is a rotational symmetric reciprocal force diagram as in Fig. 11, right. We start with a single vertex and assign forces to the emanating edges 1, 2, 3, 4 with help of a quad $\bar{1}, \bar{2}, \bar{3}, \bar{4}$ whose edges are parallel to 1, 2, 3, 4. Up to irrelevant translations, this leaves us with two degrees of freedom. We use them to choose the quad $\bar{1}, \bar{2}, \bar{3}, \bar{4}$ in a symmetric way, so that its edges are seen from a center under the same angle θ as in the original radial arrangement (Fig. 11, right). In this way, we can continue and draw a radially arranged reciprocal diagram.

This yields a simple relation between the lengths of corresponding edges and their radial distances. Let us define the radial edge distance as the distance of the edge midpoint to the rotation center. Then, as illustrated for the edge pair $\bar{6}\bar{6}$ in Fig. 11, corresponding edge vectors $\mathbf{e}_i, \bar{\mathbf{e}}_i$ and radial distances r_i, \bar{r}_i are related due to similar triangles by

$$\bar{\mathbf{e}}_i = \frac{\bar{r}_i}{r_i} \mathbf{e}_i. \quad (19)$$

This is essentially already the discrete version of equation (13). We just have to move into 3-space, take a radially arranged A-net \mathbf{s} and construct the reciprocal net $\bar{\mathbf{s}}$ via parallel edges as in the 2D case. Note that vertex stars in the A-net \mathbf{s} are planar and thus faces in the reciprocal net $\bar{\mathbf{s}}$ are planar. In the projection into a plane orthogonal to the rotational axis (top view), we have the 2D situation of Fig. 11. Due to the radial symmetry both nets are principal symmetric. They are also S-nets: the sphere center associated with vertex \mathbf{v} lies in the plane connecting \mathbf{v} with the rotation axis. If \mathbf{s} is isogonal in

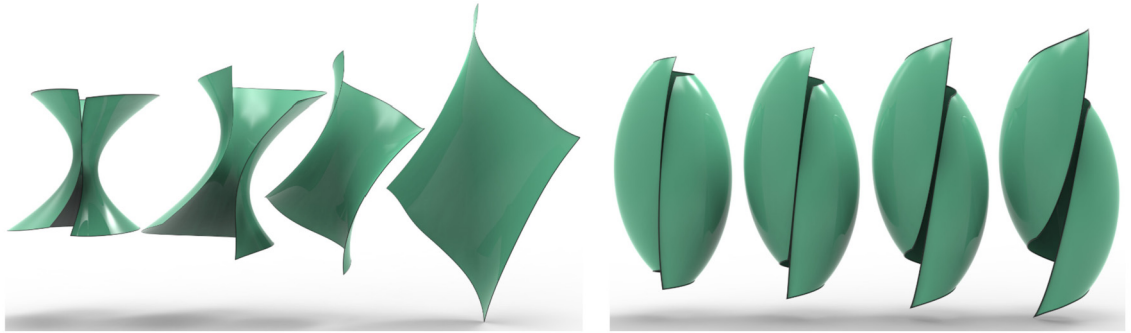


Fig. 12. Two sequences of helical CRPC surfaces, computed from a discrete rotational CRPC surface by gradually increasing the pitch p . In each sequence a is constant, left: $a = -3$, right: $a = 3$.

any discrete angle measurement, also the parallel net $\bar{\mathbf{s}}$ is to be seen as isogonal, although the definition of discrete angle is not exactly the same. A face-based angle measurement in \mathbf{s} yields a vertex-based angle measurement for $\bar{\mathbf{s}}$. We have found: *If \mathbf{s} is a discrete rotational CRPC surface with characteristic angle 2γ , then the reciprocal surface is a discrete rotational CRPC surface of positive curvature with the same characteristic angle 2γ .* Equation (19) is also valid in space, since corresponding edges are parallel. Hence, their length ratio is also seen in the top view and radial distances appear there without distortion. Fig. 11 shows that one of the two families of discrete parameter lines is in tension and the other in compression. This and the force relation (19) are well seen in Fig. 4.

3.4.2. Discrete helical surfaces

A one-parameter rigid body motion maps points $\mathbf{x}^0 \in \mathbb{R}^3$ according to $\mathbf{x}(t) = \mathbf{a}(t) + A(t) \cdot \mathbf{x}^0$, with a rotation matrix $A(t)$. The velocity vectors $\mathbf{v}(\mathbf{x}) = \dot{\mathbf{x}}(t)$ attached to the points \mathbf{x} form a linear vector field of the form

$$\mathbf{v}(\mathbf{x}) = \bar{\mathbf{c}} + \mathbf{c} \times \mathbf{x}.$$

We are interested in uniform motions. They have a time-independent velocity field, i.e. the angular velocity vector \mathbf{c} and the origin's velocity $\bar{\mathbf{c}}$ are constant. For $\mathbf{c} = 0$ one has a pure translation. For $\mathbf{c} \neq 0$, we obtain a rotation about an axis if $\mathbf{c} \cdot \bar{\mathbf{c}} = 0$ or otherwise a helical motion with pitch $p = (\mathbf{c} \cdot \bar{\mathbf{c}})/\mathbf{c}^2$. It is composed of a rotation about an axis A (direction vector \mathbf{c} , momentum vector $\bar{\mathbf{c}} - p\mathbf{c}$) and a translation parallel to A , where a rotational angle ϕ corresponds to a translation distance $p\phi$ (see e.g. Pottmann and Wallner, 2001).

A helical surface is swept by a profile curve c_p undergoing a helical motion. It contains the paths of all points of c_p . As velocity vectors are tangent to the paths, they are also tangential to the surface. Hence, a helical surface $\mathbf{s}(u, v)$ with normals $\mathbf{n}(u, v)$ fulfills the constraint

$$(\bar{\mathbf{c}} + \mathbf{c} \times \mathbf{s}) \cdot \mathbf{n} = 0.$$

With Plücker coordinates $(\mathbf{n}, \bar{\mathbf{n}}) = (\mathbf{n}, \mathbf{s} \times \mathbf{n})$ of the normal line at \mathbf{s} , one can rewrite this as

$$\bar{\mathbf{c}} \cdot \mathbf{n} + \mathbf{c} \cdot \bar{\mathbf{n}} = 0, \quad (20)$$

expressing the known characterizing property of a helical surface, namely that its normals lie in a linear line complex. For $p = \mathbf{c} \cdot \bar{\mathbf{c}} = 0$, we obtain a rotational surface. There, (20) expresses that the surface normals intersect the axis of rotation or are parallel to it (see e.g. Pottmann and Wallner, 2001). Constraint (20) can directly be applied to any discrete net with vertices \mathbf{s} and normals \mathbf{n} at vertices, in particular to C-nets.

For our application, we can adapt the coordinate system by choosing the helical axis as the third coordinate axis. Moreover, we may use an angular velocity $\omega = \|\mathbf{c}\| = 1$, so that $\mathbf{c} = (0, 0, 1)$ and $\bar{\mathbf{c}} = (0, 0, p)$. With $\mathbf{n} = (n_1, n_2, n_3)$ and $\mathbf{s} = (s_1, s_2, s_3)$, this yields the very simple constraint

$$pn_3 + s_1n_2 - s_2n_1 = 0. \quad (21)$$

Fig. 12 shows two examples, where we start from a discrete rotational CRPC surface, cut it open and gradually increase the pitch p in our optimization to obtain discrete helical CRPC surfaces. Figs. 13, 14 and 15, left, show discrete helical surfaces with their C-nets and also a family of helical paths on these surfaces. They are not directly used in the computation and visualize that one obtains helical surfaces with high precision.

3.4.3. Discrete spiral surfaces

Now we generalize rigid body motions to equiform motions, where uniform scaling is added to the moving system. With a scaling factor $\alpha(t)$ and rotation matrix $A(t)$, points are now moved via $\mathbf{x}(t) = \mathbf{a}(t) + \alpha(t)A(t) \cdot \mathbf{x}^0$ and the velocity field becomes

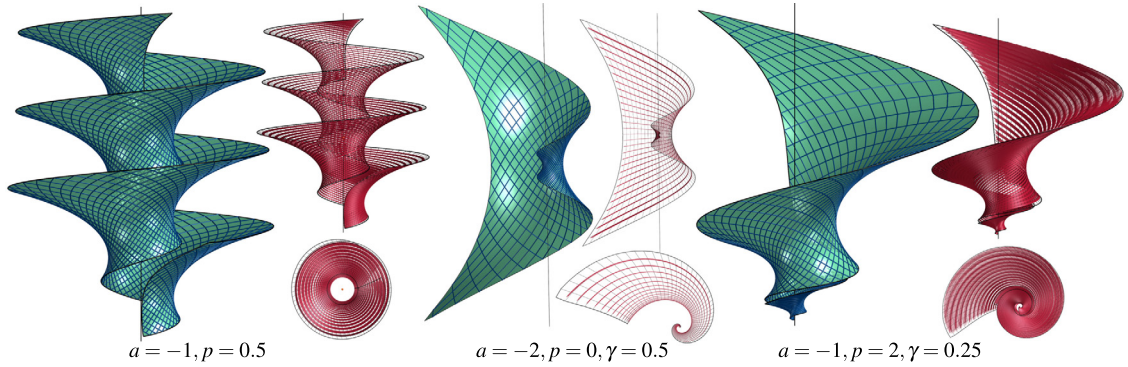


Fig. 13. Discrete helical and spiral CRPC surfaces with $a = -1, -2, -1$, their isogonal A-nets (blue) and selected motion trajectories (red). The spiral surface in the middle is symmetric to the invariant plane (through spiral center and normal to the spiral axis), while the spiral minimal surface on the right hand side is of a general type.

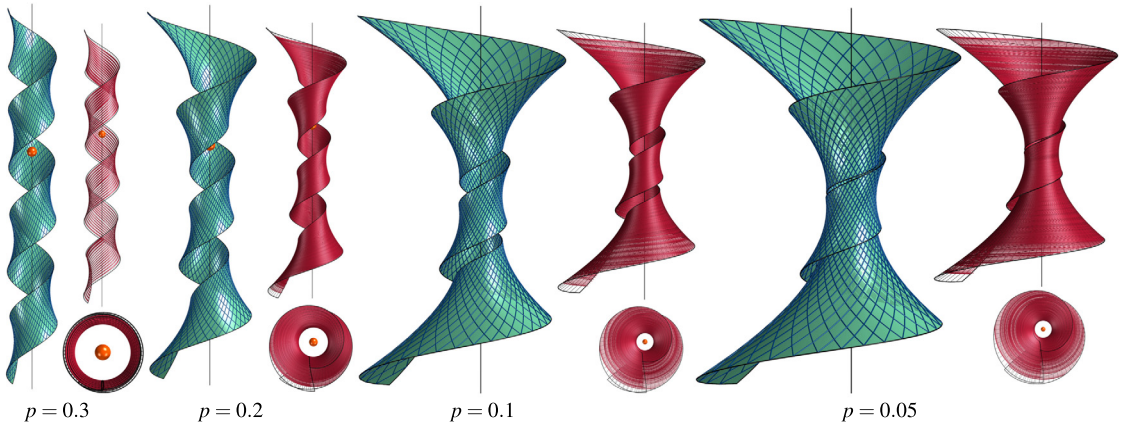


Fig. 14. Discrete helical CRPC surfaces with $a = -3$ and decreased pitch $p = 0.3, 0.2, 0.1, 0.05$. The boundary curves of the surfaces arise from the used control net and are diagonal to the net of characteristic curves.

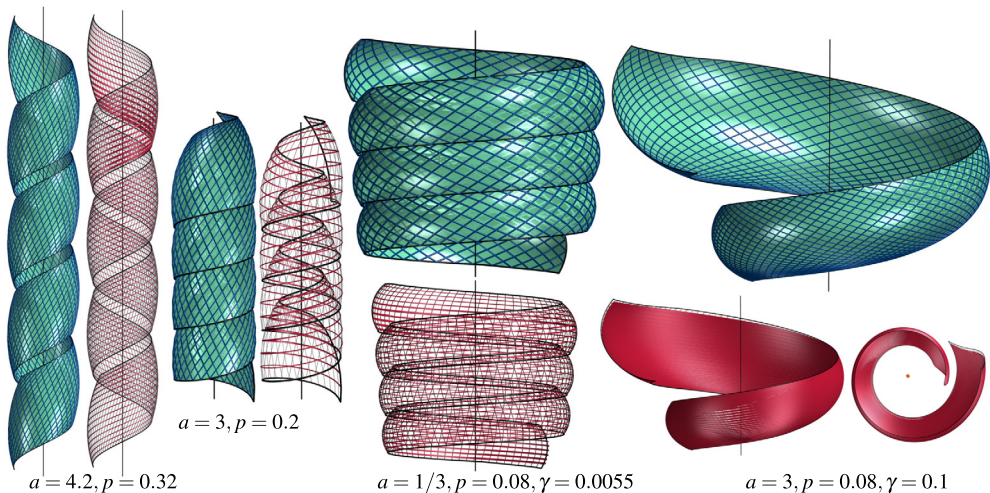


Fig. 15. Discrete helical CRPC surfaces (left two) and spiral CRPC surfaces (right two), with isogonal C-nets and motion trajectories (red).

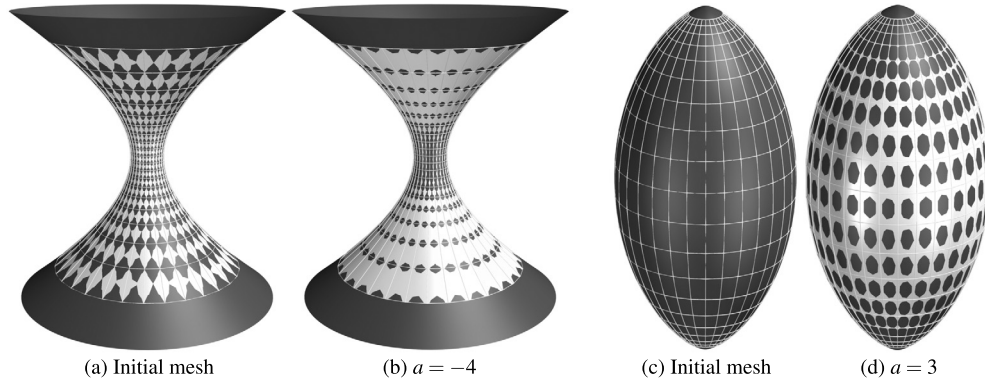


Fig. 16. Agreement of smooth (black) and discrete (white) rotational CRPC surfaces. (a),(c): Initial control meshes (for the diagonal mesh approach to discrete angle measurement) are extracted from the smooth surfaces by sampling the parameter plane at an axis-aligned square grid. (b),(d): Optimization towards exact fulfilment of our discrete CRPC surface constraints leads to tiny changes only. The Hausdorff distances of vertices in the optimized mesh to the smooth surfaces are 6.8e-5 and 1.8e-4, respectively (where diagonals of surface bounding boxes have length 1).

$$\mathbf{v}(\mathbf{x}) = \bar{\mathbf{c}} + \mathbf{c} \times \mathbf{x} + g\mathbf{x}.$$

Among the uniform equiform motions, characterized by a time-independent velocity field, we are interested in the most general ones, known as spiral motions (Wunderlich, 1967). A spiral motion fixes a point \mathbf{f} (i.e. $\mathbf{v}(\mathbf{f}) = 0$), called center, and moves points of a line A , called spiral axis, along A . Center and Plücker coordinates $(\mathbf{a}, \bar{\mathbf{a}})$ of the axis are computed as

$$\begin{aligned} \mathbf{f} &= \frac{1}{g(\mathbf{c}^2 + g^2)}(g\mathbf{c} \times \bar{\mathbf{c}} - g^2\bar{\mathbf{c}} - (\mathbf{c} \cdot \bar{\mathbf{c}})\mathbf{c}), \\ (\mathbf{a}, \bar{\mathbf{a}}) &= (\mathbf{c}, \frac{1}{\mathbf{c}^2 + g^2}(\mathbf{c}^2\bar{\mathbf{c}} - (\mathbf{c} \cdot \bar{\mathbf{c}})\mathbf{c} + g\mathbf{c} \times \bar{\mathbf{c}})). \end{aligned}$$

For $g = 0$, \mathbf{f} is at infinity and the spiral motion turns into a helical motion. If we choose $\mathbf{c} = (0, 0, 1)$, $\bar{\mathbf{c}} = (0, 0, p)$, then A is the x_3 -axis, $\mathbf{f} = (0, 0, -p/g)$, and the spiral motion reads

$$\mathbf{x}(t) = e^{gt} \begin{pmatrix} \cos t & -\sin t & 0 \\ \sin t & \cos t & 0 \\ 0 & 0 & 1 \end{pmatrix} \cdot (\mathbf{x}^0 - \mathbf{f}) + \mathbf{f}. \quad (22)$$

A curve undergoing a spiral motion generates a spiral surface. The complete spiral surface is moved in itself under the generating equiform motion and is in this sense an invariant surface. Spiral surfaces appear in nature due to exponential growth, for example in the form of certain shells (Hofer et al., 2005).

A characterization of a spiral surface follows the same principle as used for helical surfaces. Velocities are orthogonal to surface normals,

$$(\bar{\mathbf{c}} + \mathbf{c} \times \mathbf{s} + g\mathbf{s}) \cdot \mathbf{n} = 0.$$

With extended Plücker coordinates $(\mathbf{n}, \bar{\mathbf{n}}, v) = (\mathbf{n}, \mathbf{s} \times \mathbf{n}, \mathbf{s} \cdot \mathbf{n})$ of the normal line element at \mathbf{s} (normal line plus the point \mathbf{s} on it), one can rewrite this as

$$\bar{\mathbf{c}} \cdot \mathbf{n} + \mathbf{c} \cdot \bar{\mathbf{n}} + gv = 0, \quad (23)$$

expressing that the normal line elements belong to a linear complex of line elements. For a treatment of line element geometry, we refer to Odehnal et al. (2006).

In our computations, we always used $\mathbf{c} = (0, 0, 1)$, $\bar{\mathbf{c}} = (0, 0, p)$. One way to generate spiral CRPC surfaces is to start from helical CRPC surfaces, fix p and gradually change the value of g from 0 in small steps to a certain value g^* . In this way the spiral center \mathbf{f} moves from the ideal point of the x_3 -axis A to a targeted point $\mathbf{f} = (0, 0, -p/g^*)$ on the spiral axis A . The plane-symmetric types of negatively curved spiral CRPC surfaces (Fig. 13, middle) can be generated from rotational CRPC surfaces which are symmetric with respect to $x_3 = 0$. The origin takes the role of the spiral center \mathbf{f} . We set $p = 0$ and then gradually increase the spiral parameter g .

4. Results and discussion

4.1. Checking the quality of discrete models

The explicit results on smooth rotational CRPC surfaces provide a test scenario for the quality of our geometric discretization. Fig. 16 compares smooth rotational CRPC surfaces with their discrete counterparts, revealing an excellent agreement.

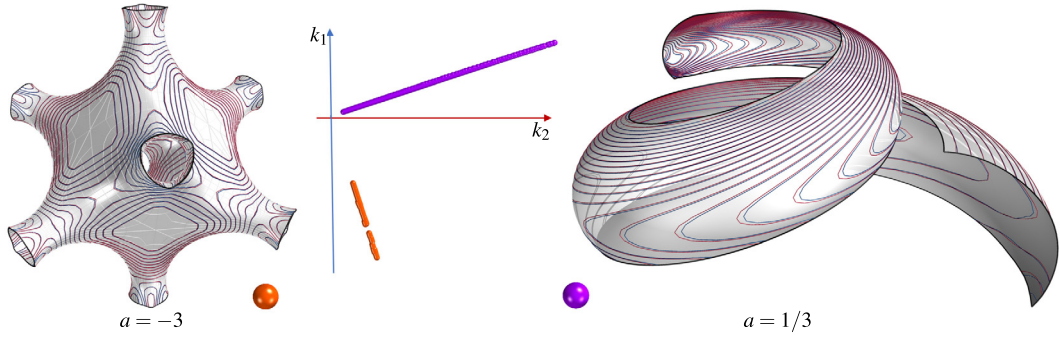


Fig. 17. Alignment of isolines of principal curvatures κ_1 and κ_2 , respectively (blue,red) on two discrete CRPC surfaces. The estimated principal curvature values yield points on the correct straight lines in the (k_2, k_1) -plane.

Table 1
Optimization statistics to selected Figures of different complexity.

Fig.	vertices	variables	T/iter	err=F(X _{min})
13-left	6231	101320	4.71 s	7.1e-8
15-right	2856	76625	2.99 s	6.8e-9
17-left	6330	85963	4.83 s	1.4e-12
17-right	6755	160732	8.12 s	2.1e-11
19-top left	1520	20161	5.83 s	3.7e-14
20-right	4244	55481	2.77 s	3.9e-10
18-3rd	6231	101320	4.21 s	1.5e-11
21-2nd row-right	2085	26836	0.83 s	1.5e-12
21-3rd row-left	6330	85963	4.88 s	1.4e-12
21-4th row-right	3254	42907	1.60 s	2.1e-15
22-top left	3010	40383	1.60 s	2.9e-12

Fig. 17 checks the quality of the presented discrete CRPC surfaces with the fact that on a Weingarten surface (to any relation $f(\kappa_1, \kappa_2) = 0$), the isolines of κ_1 agree with those of κ_2 . Also, we demonstrate that the relation is the correct one, since points (κ_1, κ_2) nicely arrange along straight lines $\kappa_1 = a\kappa_2$ in the plane. Curvatures have been estimated via normal cycles (Cohen-Steiner and Morvan, 2003).

4.2. Implementation details and parameters

The algorithms have been implemented in Python and tested on an Intel Xeon E5-2687W 3.0 GHz processor. Typically around 10-15 iterations have been necessary to achieve convergence, depending on the quality of the initialization. In all examples, we set $\epsilon = 0.001$. The fairness weight μ is set to 0.005 during the first 5-10 iterations and we use $\mu = 0$ in the last 5 iterations. For all meshes, the length of the bounding box diagonals equals 1. Further details are provided in Table 1.

4.3. Exploring the shape space of general CRPC surfaces

Let us now play a bit with the available tools to get some initial ideas about the shape variety in the space of all CRPC surfaces.

Computational design of CRPC surfaces with a freeform appearance can start from the special ones discussed above. This is illustrated in Fig. 19 with a design tool that allows the user to select some mesh vertices and move them to new locations. These may be conflicting with the CRPC constraints and are therefore implemented as soft constraints. We simply add the squared distance of original and target location, multiplied with a small weight, to the objective function and let the weight fade away in later iterations.

Another way to get a larger shape is by joining pieces of CRPC surfaces and optimizing the resulting mesh so that initial defects along the joints disappear (see Fig. 20).

An interesting question concerns the shape space of minimal surfaces within the larger space of CRPC surfaces. Can one start with an orthogonal A-net ($a = -1$) and continuously walk away from that shape by changing the value of a ? The main question is whether one can keep the combinatorics of the net. Our experiments have been successful (see Figs. 18 and 21), even with high numerical accuracy (Table 1). The A-nets in Fig. 21 have been obtained by taking S-conical minimal surfaces (Bobenko et al., 2015) as initial control nets. It remains open whether or under which conditions a minimal surface of given combinatorics of its A-net (principal net) can be turned into a CRPC surface of the same combinatorics by gradually changing the principal curvature ratio a .

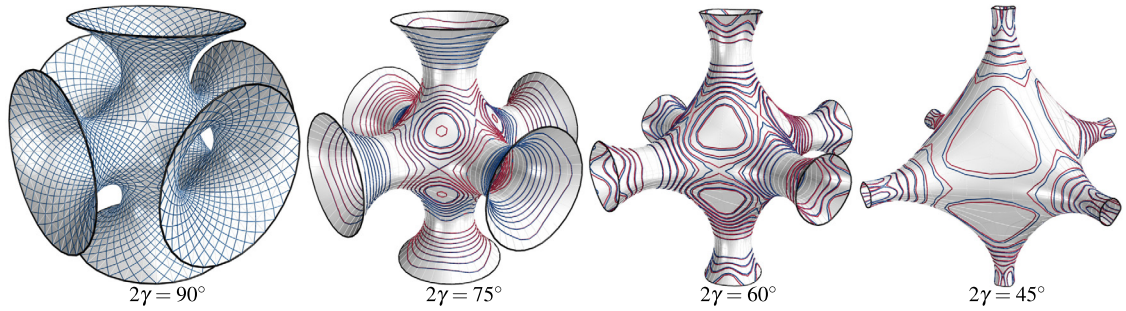


Fig. 18. Discrete negatively curved CRPC surfaces with selected curvature isolines, obtained from a discrete minimal surface (A-net with $2\gamma = 90^\circ$) by keeping the mesh combinatorics and optimizing for other angles in the A-net.

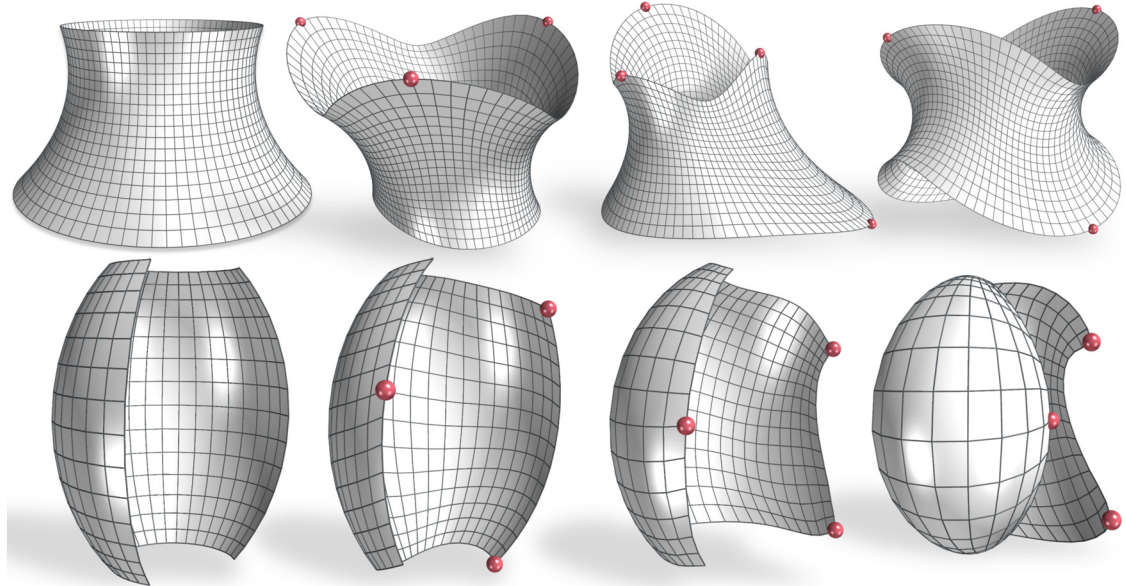


Fig. 19. Modeling CRPC surfaces through mesh editing. We start from meshes representing rotational CRPC surfaces (top left: $\gamma = 38.5^\circ$, bottom left: $a = 2$) and drag some vertices to new locations. The curvature ratio a is fixed and the shown meshes are the control meshes for the diagonal mesh approach.

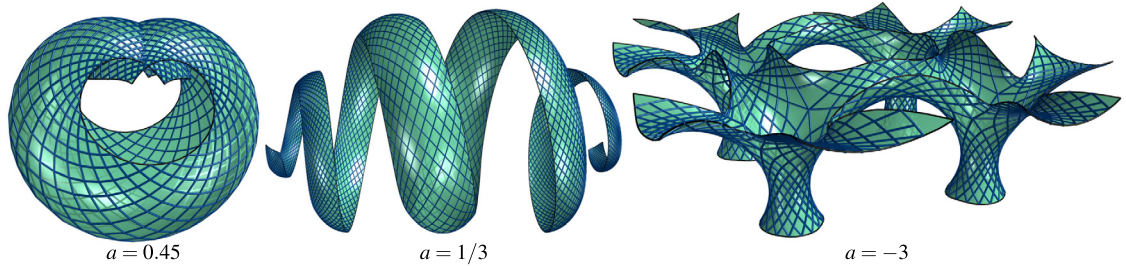


Fig. 20. Discrete CRPC surfaces, optimized after joining copies of smaller CRPC meshes. Left: $a = 0.45$, initial piece from Fig. 1. Center: $a = 1/3$, initial shape from Fig. 17, right. Right: Input mesh obtained from Fig. 18 with $2\gamma = 60^\circ$ by cutting it, joining four copies and editing the whole shape.

4.4. Singularities

Looking at our parts of helical CRCP surfaces with $a > 0$ (Fig. 12 and Fig. 15), one might ask how these surfaces can be extended towards the helical axis. The answer is that they develop singular curves, which are of course helices. We cannot show them in our discrete approach, since extension towards and beyond a singular curve is prevented by the fairness term. However, in our ongoing research we obtained a parameterization of helical CRPC surfaces from which we can derive the existence of singular curves. Most likely, these are also present in more general positively curved CRPC surfaces.

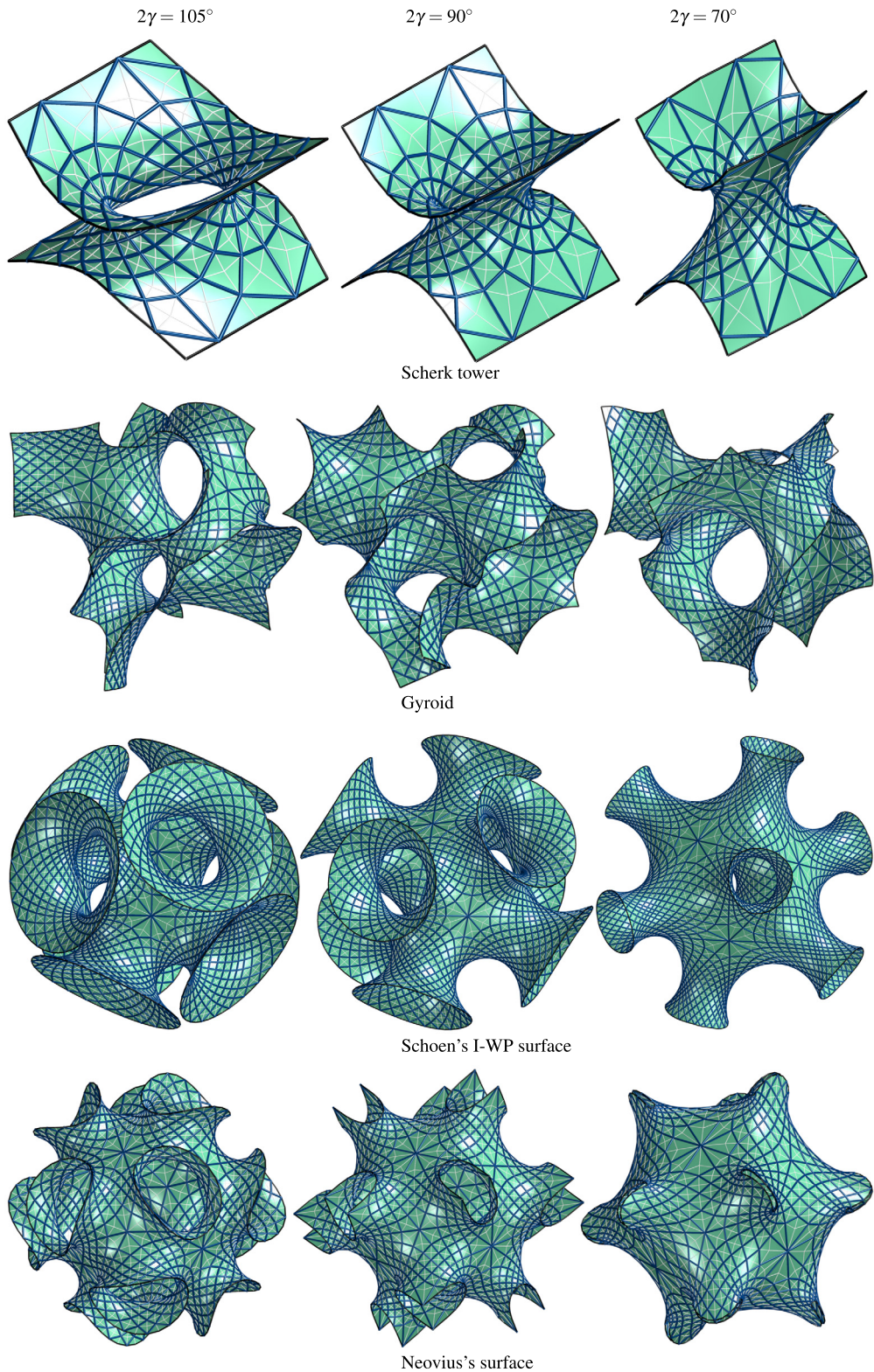


Fig. 21. Discrete CRPC surfaces obtained from selected classical minimal surfaces (center) by changing the angle γ in the A-net.

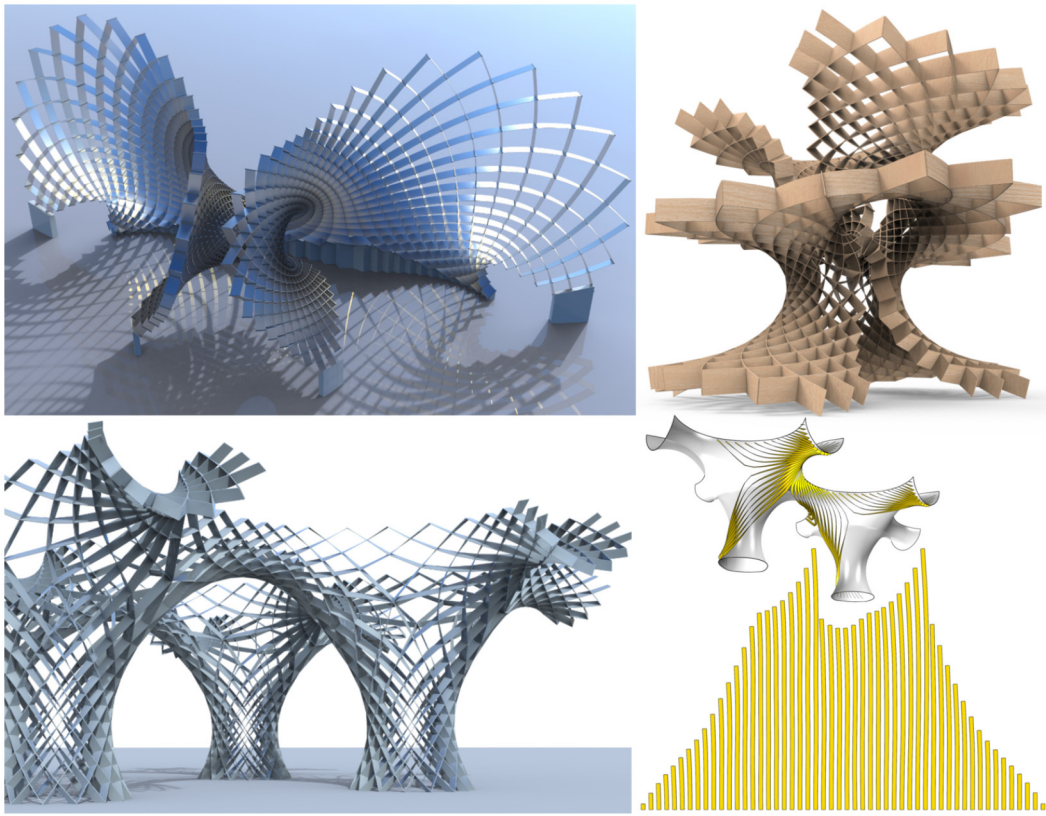


Fig. 22. Asymptotic gridshells, formed by developable surface strips with a straight development, that are attached orthogonally to negatively curved CRPC surfaces along selected asymptotic curves. Top: Gridshells from minimal surfaces, $a = -1$. Bottom: Gridshell with node angle $\pi/3$, $a = -3$. Even in this coarse discrete model for the strips, their development is nearly straight.

Another type of singularities to be discussed are those of the C-nets. In the smooth setting, they correspond to umbilics. For surfaces different from the sphere ($a \neq 1$), they can only be flat points ($\kappa_1 = \kappa_2 = 0$) or isolated singular points ($\kappa_1 = \kappa_2 = \infty$). The behavior of Weingarten surfaces, in particular CRPC surfaces, at umbilics has been studied by Hopf (1951) under the additional assumption that the surfaces are analytic. There, he found that a closed CRPC surface can only have topological genus 0 and – if different from a sphere – it has exactly two flat points and $a = (2n + 1)^{\pm 1}$, $n \in \mathbb{N}$. The only known surfaces of that type are rotational. We used our discrete model for a simple experiment with the goal to obtain discrete closed non-rotational CRPC surfaces. Initializing from a discrete rotational CRPC surface with $a = 1/3$ and editing it by relocating some mesh vertices (but keeping the surface closed) the algorithm always converged to a rotational shape, even when removing a small cap around the two mesh singularities. Maybe closed CRPC surfaces are always rotational?

In the discrete setting, the singularities of the net correspond to extraordinary vertices (valence $\neq 4$). As for principal meshes, their valence has to be even if all faces around them are quads. We do not apply constraints there. We also do not use fairness terms to three consecutive points where the middle one is an extraordinary vertex.

4.5. Applications in architecture and design

A straight strip of flat material which can be bent but not stretched can be attached orthogonally to a surface only along an asymptotic curve. This has already been pointed out by Finsterwalder (1899) and forms a basic ingredient to the asymptotic gridshells of Schling (2018). Since negatively curved CRPC surfaces are isogonal A-nets, they are appropriate reference surfaces for asymptotic gridshells with a constant node angle (see also Jiang et al., 2020). Fig. 22 shows examples computed with our design tool. The one on the upper right is not meant as an architectural structure, but an artistic design.

Discrete C-nets for positively curved CRPC surfaces are quad meshes with planar faces that can form the basis of architectural skins. Due to the constant angle and principal symmetry they have an appealing and well-balanced visual appearance (Fig. 1) that may be preferred over structures from principal meshes. An example of a built structure with a principal symmetric arrangement of flat quad panels on a rotational surface is provided by the Osaka Maritime Museum.

4.6. Conclusion and future research

We showed that characteristic nets are well suited for studying and computing CRPC surfaces, since these are characterized through isogonal C-nets. In the smooth setting, this led to a few additional insights on the known rotational CRPC surfaces. We then focused on discrete CRPC surfaces and introduced an approach for their computational design.

There is a simple extension of CRPC surfaces which we did not mention so far. It concerns the *offsets of CRPC surfaces*. Since a surface and all its offsets share their principal curvature centers at corresponding points, the offsets of CRPC surfaces are Weingarten surfaces with a *linear relation* $a\rho_1 + b\rho_2 = c$ between their principal curvature radii $\rho_i = 1/\kappa_i$. Discrete models are most easily obtained by offsetting discrete CRPC surfaces via their discrete normals (through sphere centers). The offsets of C-nets are however no longer C-nets.

Since CRPC surfaces did not yet receive much interest, there are many directions for future research, including the following ones.

- (1) So far, the only known explicit representations of CRPC surfaces concern rotational ones. Recently, we could also solve the ordinary differential equation for helical CRPC surfaces, not using a characteristic parameterization. Maybe one can even handle the more involved case of spiral CRPC surfaces, but there is nothing beyond these special surfaces.
- (2) We hope that our tools will help to get a better understanding of the possible shapes of CRPC surfaces and will lead to conjectures for deeper mathematical studies. We raised the questions of closed CRPC surfaces, where we failed to get discrete ones beyond rotational shapes. We also pointed to the probably always present singular curves in more general CRPC surfaces of positive curvature.
- (3) Another question concerns the shape space of negatively curved CRPC surfaces which contains the minimal surfaces. Can we move away from a minimal surface by changing to $a \neq -1$, and can we keep the combinatorics of the C-net, as it worked numerically in Figs. 18 and 21?
- (4) Again looking at the special case of minimal surfaces, can CRPC surfaces be generated from a given boundary? A computational approach to this problem would benefit from a discrete model that is not relying on a special geometric parameterization like ours.
- (5) While there is a wealth of results on the discrete theory of A-nets (Bobenko and Suris, 2008), we are not aware of similar studies for S-nets, or at least for C-nets in the case of positive curvature (Q-nets + S-nets).
- (6) For architectural applications one also needed to study force equilibrium under the influence of gravity and the geometry of the supporting structure, especially for realizations as in Fig. 1.

CRediT authorship contribution statement

Hui Wang: development and implementation of algorithms, visualization, original draft preparation. **Helmut Pottmann:** conceptualization, methodology, final writing.

Declaration of competing interest

The authors declare that they have no known competing financial interests or personal relationships that could have appeared to influence the work reported in this paper.

Acknowledgements

We are very grateful to Stefan Sechelmann for sharing his models of discrete minimal surfaces and to Christian Müller for stimulating discussions. This research has been supported by KAUST baseline funding (grant BAS/1/1679-01-01) and has been performed within the research program of the SFB-Transregio *Discretization in Geometry and Dynamics* (grant I 2978 of the Austrian Science Fund).

References

- Blaschke, W., 1930. Differentialgeometrie 1, 3rd edition. Springer, Berlin.
- Bobenko, A., König, B., Hoffmann, T., Sechelmann, S., 2015. S-conical minimal surfaces. Towards a unified theory of discrete minimal surfaces. TU Berlin. Preprint.
- Bobenko, A.I., Suris, Yu.B., 2008. Discrete Differential Geometry. Integrable Structure. Graduate Studies in Mathematics, vol. 98. American Mathematical Society.
- Cohen-Steiner, D., Morvan, J.-M., 2003. Restricted Delaunay triangulations and normal cycle. In: Proc. Symposium on Computational Geometry, pp. 312–321.
- Finsterwalder, S., 1899. Mechanische Beziehungen bei der Flächendeformation. Jahresber. Dtsch. Math.-Ver. 6, 43–90.
- Hofer, M., Odehnal, B., Pottmann, H., Steiner, T., Wallner, J., 2005. 3d shape recognition and reconstruction based on line element geometry. In: Intl. Conference on Computer Vision (ICCV), vol. 2. IEEE, pp. 1532–1538.
- Hopf, H., 1951. Über Flächen mit einer Relation zwischen den Hauptkrümmungen. Math. Nachr. 4, 232–249.
- Jiang, C., Wang, C., Rist, F., Wallner, J., Pottmann, H., 2020. Quad-mesh based isometric mappings and developable surfaces. ACM Trans. Graph. (TOG) 39 (4), 128.
- Jiang, C., Wang, C., Schling, E., Pottmann, H., 2021b. Computational design and optimization of quad meshes based on diagonal meshes. In: Advances in Architectural Geometry.

- Jiang, C., Wang, H., Inza, V.C., Dellinger, F., Rist, F., Wallner, J., Pottmann, H., 2021a. Using isometries for computational design and fabrication. *ACM Trans. Graph.* (TOG) 40 (4), 42.
- Jimenez, M.R., 2021. Note on surfaces of revolution with an affine-linear relation between their curvature radii. *ArXiv eprint. arXiv:2105.10320*.
- Jimenez, M.R., Müller, C., Pottmann, H., 2020. Discretizations of surfaces with constant ratio of principal curvatures. *Discrete Comput. Geom.* 63 (3), 670–704.
- Kühnel, W., 2013. Differentialgeometrie. Aufbaukurs Mathematik. Springer Spektrum, Wiesbaden.
- López, R., 2008. Linear Weingarten surfaces in Euclidean and hyperbolic space. *Mat. Contemp.* 35, 95–113.
- Lopez, R., Pampano, A., 2020. Classification of rotational surfaces in Euclidean space satisfying a linear relation between their principal curvatures. *Math. Nachr.* 293, 735–753.
- Michell, A.G.M., 1904. The limit of economy of material in frame-structures. *Philos. Mag.*, Ser. VI 8, 589–597.
- Mladenov, I.M., Oprea, J., 2003. The Mylar balloon revisited. *Am. Math. Mon.* 110 (9), 761–784.
- Mladenov, I.M., Oprea, J., 2007. The Mylar balloon: new viewpoints and generalizations. In: *Geometry, Integrability and Quantization*. Softex, Sofia, pp. 246–263.
- Müller, E., 1921. Relative Minimalflächen. *Monatshefte Math. Phys.* 31, 1–19.
- Odehnal, B., Pottmann, H., Wallner, J., 2006. Equiform kinematics and the geometry of line elements. *Beitr. Algebra Geom.* 47 (2), 567–582.
- Pellis, D., Wang, H., Kilian, M., Rist, F., Pottmann, H., Müller, C., 2020. Principal symmetric meshes. *ACM Trans. Graph.* (TOG) 39 (4), 127.
- Pellis, D., Kilian, M., Pottmann, H., Pauly, M., 2021b. Computational design of Weingarten surfaces. *ACM Trans. Graph.* (TOG) 40 (4), 114.
- Pellis, D., Kilian, M., Wang, H., Jiang, C., Müller, C., Pottmann, H., 2021a. Architectural freeform surfaces designed for cost-effective paneling mold re-use. In: *Advances in Architectural Geometry*.
- Pottmann, H., 1982. Zwei Verallgemeinerungen der Böschungslinien. *Österreich. Akad. Wiss. Math.-Natur. Kl. Sitzungsber.* II 191 (8–9), 311–324.
- Pottmann, H., Wallner, J., 2001. Computational Line Geometry. Springer.
- Rabinovich, M., Hoffmann, T., Sorkine-Hornung, O., 2018. Discrete geodesic nets for modeling developable surfaces. *ACM Trans. Graph.* (TOG) 37 (2), 16.
- Riveros, C.M.C., Corro, A.M.V., 2012. Surfaces with constant Chebyshev angle. *Tokyo J. Math.* 35 (2), 359–366.
- Riveros, C.M.C., Corro, A.M.V., 2013. Surfaces with constant Chebyshev angle II. *Tokyo J. Math.* 36 (2), 379–386.
- Sauer, R., 1970. Differenzengeometrie. Springer-Verlag, Berlin-New York.
- Schling, E., 2018. Repetitive structures. Ph.D. thesis. TU Munich.
- Schling, E., Kilian, M., Wang, H., Schikore, D., Pottmann, H., 2018. Design and construction of curved support structures with repetitive parameters. In: Hesselgren, L., Kilian, A., Malek, S., Olsson, K.-G., Sorkine-Hornung, O., Williams, C. (Eds.), *Advances in Architectural Geometry*. Klein Publishing Ltd., pp. 140–165.
- Stäckel, P., 1896. Beiträge zur Flächentheorie. III. Zur Theorie der Minimalflächen. *Leipziger Berichte*, pp. 491–497.
- Strubecker, K., 1969. Differentialgeometrie II. Walter de Gruyter, Berlin.
- Tang, C., Sun, X., Gomes, A., Wallner, J., Pottmann, H., 2014. Form-finding with polyhedral meshes made simple. *ACM Trans. Graph.* (TOG) 33 (4), 70.
- Tellier, X., 2020. Morphogenesis of curved structural envelopes under fabrication constraints. Ph.D. thesis. Univ. Paris-Est.
- Tellier, X., Douthe, C., Hauswirth, L., Baravel, O., 2020. Caravel meshes: a new geometrical strategy to rationalize curved envelopes. *Structures* 28, 1210–1228.
- Wang, H., Pellis, D., Rist, F., Pottmann, H., Müller, C., 2019. Discrete geodesic parallel coordinates. *ACM Trans. Graph.* (TOG) 38 (6), 173.
- Weingarten, J., 1861. Über eine Klasse aufeinander abwickelbarer Flächen. *J. Reine Angew. Math.* 59, 382–393.
- Wunderlich, W., 1950. Raumkurven, die pseudogeodätische Linien eines Zylinders und eines Kegels sind. *Compos. Math.* 8, 169–184.
- Wunderlich, W., 1952. Beitrag zur Kenntnis der Minimalschraubflächen. *Compos. Math.* 10, 297–311.
- Wunderlich, W., 1954. Beitrag zur Kenntnis der Minimalspiralfächen. *Rend. Math.* 13, 1–15.
- Wunderlich, W., 1967. Darstellende Geometrie II. Bibliographisches Institut, Mannheim.